Computer Methods in Applied Mechanics and Engineering 432 (2024) 117398

Contents lists available at ScienceDirect

Comput. Methods Appl. Mech. Engrg.

journal homepage: www.elsevier.com/locate/cma

An immersed multi-material arbitrary Lagrangian–Eulerian finite element method for fluid–structure-interaction problems☆

Zixian Sun, Zhixin Zeng, Jiasheng Li, Xiong Zhang *

School of Aerospace Engineering, Tsinghua University, Beijing 100084, PR China

ARTICLE INFO

Keywords:
Multi-material arbitrary Lagrangian Eulerian method
Finite element method
Immersed boundary method
Fluid–structure interaction

ABSTRACT

Fluid–structure-interaction (FSI) phenomena are widely concerned in engineering practice and challenge current numerical methods. In this article, the finite element method is strongly coupled with the multi-material arbitrary Lagrangian–Eulerian (MMALE) method to develop a monolithic FSI method named the immersed multi-material arbitrary Lagrangian–Eulerian finite element method (IALEFEM). By immersing the finite elements in the MMALE computational grid, the fluid–solid interface is directly tracked by the element boundary with accurate normal directions. The fluid–structure-interaction is implicitly implemented by assembling the nodal variables and updating the Lagrangian momentum equation on the MMALE grid. Combining the advantages of both MMALE and FEM with the immersed boundary method, the IALEFEM is effective for solving complicated FSI problems with multi-material fluid flow. A slip fluid–structure-interaction method is also proposed to enhance the computational accuracy in simulating FSI problems with significantly different velocity fields. The accuracy and effectiveness of the IALEFEM are verified and validated by several benchmark numerical examples including the shock-cylinder obstacle interaction, flexible panel deformation induced by shock wave, dam break problem with large structural deformation, water entry of a wedge, fragmentation of a cylinder shell induced by blast, response of elastic plate subjected to spherical near-field explosion and structural damage of open-frame building under blast loading.

1. Introduction

Fluid–structure-interaction (FSI) problems are widely concerned in science and engineering fields including porous media [1–5], ocean engineering [6–8], shock-structure-interaction [9–11], nuclear [12–14] and water entry [15–17]. In order to explore the corresponding mechanism and conduct practical engineering applications, extensive efforts have been made in recent decades and remarkable progress has been achieved. However, complicated FSI problems always involve shock discontinuity, multi-phase flow and complex geometry of structures with dynamic failure, which challenge current theoretical and experimental methods. Therefore, developing accurate and powerful numerical algorithms is of great significance.

According to different fluid–structure coupling schemes, present numerical methods can be mainly divided into two categories. The first category includes methods where the fluid and solid meshes are overlapped with each other and interface conditions are applied on the fluid and solid respectively. These partitioned methods solve the fluid and solid governing equations alternately and allow using common mesh-based methods such as the finite element method (FEM), finite difference method (FDM) and finite volume method (FVM) with specifically designed codes on the different fields. Noh [18] developed the coupled Eulerian–Lagrangian

☆ Supported by the National Natural Science Foundation of China (12172192).
* Corresponding author.
E-mail address: xzhang@tsinghua.edu.cn (X. Zhang).

https://doi.org/10.1016/j.cma.2024.117398
Received 11 May 2024; Received in revised form 13 September 2024; Accepted 13 September 2024
Available online 18 September 2024

(CEL) code and applied it on many engineering problems. Chen et al. [19] presented a novel multi-resolution fluid–structure interaction (FSI) solver with the weakly compressive smoothed particle hydrodynamics (WCSPH) method adopted for fluid and FEM beam adopted for structures. Zhang et al. [20] effectively simulated structural damage subjected to near-field underwater explosions by coupling the compressible SPH method with the RKPM shell. Zheng et al. [21] coupled the phase-field lattice Boltzmann and the convected particle-domain interpolation-based material point method (MPM) to simulate multiphase fluid–solid bidirectional interaction problems. Several interface algorithms such as cut-cell [22] and level-set methods [23] are also presented to solve FSI problems. However, the interface conditions are applied asynchronously, which makes the partitioned methods sometimes unstable and causes errors near the fluid–structure-interaction interface. Förster et al. [24] studied the artificial added mass effect related to instabilities within sequentially staggered partitioned FSI simulations.

In another FSI methodology, the fluid and solid regions are solved simultaneously by assembling the monolithic governing equations for the whole computational domain. The fluid–structure interface is directly and accurately tracked with the interface nodes in the Lagrangian frame. The Lagrangian description of structural motion combined with the arbitrary Lagrangian-Eulerian (ALE) [25–29] description of fluid is the preferred approach when the interface motions are not excessive [30]. The space–time finite element methods [31–33] are also the typical representatives which can track the fluid–structure interfaces with relatively coarse mesh. In many monolithic FSI methods, the fluid mesh conforms to the structural domain and different meshes of fluid and solid share common nodes on the boundary. Dutta et al. [34] proposed a monolithic finite-element-based strategy for FSI problems with hyperelastic deformation of solid, incompressible fluid and electrostatics. Another kind of monolithic methods computes the monolithic FSI equations by using an iterative process to solve fluid and solid partitioned systems which are equivalent to solving FSI equations using algebraic methods like block Newton or Gauss–Seidel methods. González et al. [30] proposed a novel variant of monolithic methods with the localized Lagrange multipliers (LLM) method which introduces an intermediate surface with its own degrees of freedom. Peery et al. [35] presented the multi-material arbitrary Lagrangian-Eulerian (MMALE) method which [35] allows multiple materials to exist in a single cell and simulates complex multi-material interface of fluid well with the help of MOF method [36,37]. Chen et al. [38] enhanced the efficiency and robustness of MMALE and combined the MMALE method and FEM with common nodes to simulate complex FSI problems involving multi-material flow [39]. Although FSI boundary conditions are conveniently implemented on the monolithic methods with conformed fluid–solid interface, they have difficulties in dealing with FSI problems with extreme deformation and fragmentation of solid as the conformed interface leads to distorted grid which will terminate the calculation.

The immersed boundary method (IB) originally proposed by Peskin [40] in the 1970s is suitable to solve FSI problems with large structural motion and deformation. Based on the immersed boundary method, other formulations were proposed like immersed finite element method (IFEM) by Zhang et al. [41–44] and immersed smoothed finite element method (IS-FEM) by Jiang et al. [45] for the solution of the interaction problems between the complex fluid flow in fixed grid and deformable finite element structure. Ni et al. [11] proposed a novel immersed boundary method based on the Lagrangian multiplier and successfully applied it to the analysis of structures under blast loading. Li et al. [46] proposed an immersed finite element material point method by combining an improved incompressible material point method with the FEM to deal with free surface fluid–structure interaction problems. The immersed boundary method can also be adopted in the monolithic FSI methods. Schott et al. [47] submerged the ALE fluid patch grid surrounding the solid surface into the Eulerian background fluid domain and presented a monolithic approach with hybrid Eulerian-ALE fluid weakly coupled by the cut FEM method. Kim et al. [48] developed a surrounding cell method for the submerged solid and proposed a cell-based smoothed finite element method to deal with FSI problems with arbitrary motion of solid. The MPM also solves the Lagrangian momentum equation on the background grid which can be easily coupled with mesh-based methods. Kan and Zhang [49] presented a monolithic MMALE particle method by coupling staggered MMALE and MPM. Sun et al. [50] developed a localized subdomain smoothing MMALE particle method for efficient and accurate simulations of large scale FSI problems. However, the computational accuracy of the solid region is less than second-order with the particle integration and cell crossing noise is generated in the MPM.

The FEM is still the most common and effective method for simulating solids and has significant advantages in dealing with finite deformation of solid. In this study, the finite element method is combined with the MMALE method to develop a monolithic FSI method named the immersed MMALE finite element method (IALEFEM). By immersing the finite elements in the MMALE computational grid, the solid–fluid interface is directly tracked by the element boundary with accurate normal directions. Meanwhile accurate simulation of multi-phase fluid flow and precise tracing of multi-phase fluid interface can also be realized. The fluid–structure-interaction is implicitly implemented by assembling the nodal variables and updating the Lagrangian momentum equation on the MMALE grid. Combining the advantages of both MMALE and FEM with the immersed boundary method, the IALEFEM is effective for solving complicated FSI problems with multi-material fluid flow. Compared with the coupled MMALE-FEM by Chen et al. [39], the fluid grid does not conform to the solid boundary in IALEFEM, which makes the mesh rezoning easily to conduct and enhances the computational efficiency significantly. Compared with the immersed MMALE material point method [49], hexahedral elements, solid shell elements and other elements in FEM can be applied to the discretization of solid region which will remove the cell crossing noise of MPM and improve the computational accuracy and stability.

The paper is structured as follows. Governing equations of the fluid and solid domains are given in Section 2. Then the multi-material arbitrary Lagrangian Eulerian method are briefly introduced in Section 3. Section 4 presents the detailed formation of the proposed IALEFEM including the Lagrangian phase and Euler phase. Validations and benchmark simulations are presented in Section 5. Finally, conclusions are drawn in Section 6.

2. Governing equations

The MMALE and FEM both solve the weak form of momentum equation in an updating Lagrangian scheme. The governing equations of continuum mechanics in the updated Lagrangian frame are

$$\begin{aligned} \dot{\rho} &= -\rho \dot{u}_{i,i} \\ \rho \ddot{u}_i &= \sigma_{ji,j} + \rho b_i \\ \rho \dot{e} &= \dot{\varepsilon}_{ij} \sigma_{ij} \end{aligned} \tag{1}$$

where ρ is the current density, the overdot denotes derivative with respect to time, e is the specific internal energy, the subscripts i and j indicate the components of the spatial variables following the Einstein convention, u_i is the displacement, b_i is the body force per unit mass, σ_{ij} is the Cauchy stress and ε_{ij} is the Cauchy strain. Note that the comma in the subscript denotes the derivative.

The kinematic condition and boundary/initial conditions are given by

$$\dot{\varepsilon}_{ij} = \frac{1}{2}(\dot{u}_{i,j} + \dot{u}_{j,i}) \tag{2}$$

$$n_j \sigma_{ji} = \bar{t}_i, \ \boldsymbol{x} \in \Gamma_t \tag{3}$$

$$u_i = \bar{u}_i, \ \boldsymbol{x} \in \Gamma_u \tag{4}$$

$$u_i(\boldsymbol{X}, 0) = u_{i0}(\boldsymbol{X}), \quad \dot{u}_i(\boldsymbol{X}, 0) = \dot{u}_{i0}(\boldsymbol{X}) \tag{5}$$

where Γ_u and Γ_t denote the displacement boundary and traction boundary of the material domain Ω, respectively, n_j is the unit normal of the boundary Γ_t, $\boldsymbol{x}$ is the spatial coordinate in the current configuration, $\boldsymbol{X}$ is the material coordinate in the initial configuration, $\bar{u}_i$ and $\bar{t}_i$ are the prescribed displacement and traction, respectively, u_{i0} and $\dot{u}_{i0}$ are the initial displacement and initial velocity, respectively.

The weak form equivalent to the momentum equation and traction boundary condition is given as

$$\int_\Omega \rho \ddot{u}_i \delta u_i \mathrm{d}\Omega + \int_\Omega \rho \sigma^{\mathrm{s}}_{ij} \delta u_{i,j} \mathrm{d}\Omega - \int_\Omega \rho b_i \delta u_i \mathrm{d}\Omega - \int_{\Gamma_t} \rho \bar{t}^{\mathrm{s}}_i \delta u_i \mathrm{d}\Gamma = 0 \tag{6}$$

where $\sigma^{\mathrm{s}}_{ij} = \sigma_{ij}/\rho$ is the specific stress, $\bar{t}^{\mathrm{s}}_i = \bar{t}_i/\rho$ is the specific traction and $\delta u_i \in \mathscr{R}_0 (\mathscr{R}_0 = \{\delta u_i | \delta u_i \in C^0, \delta u_i|_{\Gamma_u} = 0\})$ is the virtual displacement.

Discretizing the computational domain with MMALE cells and FEM elements, the displacement field $u_i(\boldsymbol{x})$ is approximated with the grid nodal displacement u_I as

$$u_i(\boldsymbol{x}) = \sum_I N_I(\boldsymbol{x}) u_I \tag{7}$$

where $N_I(\boldsymbol{x})$ is the grid nodal shape function and the trilinear shape function is expressed as $N_I = \frac{1}{8}(1 + \xi_I \xi)(1 + \eta_I \eta)(1 + \zeta_I \zeta)$ for three dimensional 8-node hexahedral element with $\xi, \eta, \zeta \in [-1, 1]$ denoting the natural coordinates. The approximate function constructed by the trilinear shape function has linear completeness and satisfies second-order convergence in displacement space. Thus the one point Gauss quadrature can meet the requirement of second-order convergence rate for the displacement.

Invoking the arbitrariness of the virtual displacement δu_i leads to

$$m_I \dot{v}_{iI} = f_{iI} + \tilde{f}_{iI}, \ \forall I \notin \Gamma_u \tag{8}$$

where m_I is the mass of node I, v_{iI} is the velocity of node I, f_{iI} and $\tilde{f}_{iI}$ are the internal force and external force of node I, respectively. The lumped nodal mass is calculated as

$$m_I = \int_\Omega \rho N_I(\boldsymbol{x}) \mathrm{d}\Omega \tag{9}$$

The internal nodal force and external nodal force are calculated as

$$f_{iI} = -\int_\Omega N_{I,j}(\boldsymbol{x}) \sigma_{ij} \mathrm{d}\Omega \tag{10}$$

$$\tilde{f}_{iI} = \int_\Omega N_I(\boldsymbol{x}) \rho b_i \mathrm{d}\Omega + \int_{\Gamma_t} N_I(\boldsymbol{x}) \bar{t}_i \mathrm{d}\Gamma \tag{11}$$

The equation of state (EOS) is used for the fluid to close the governing equations. The Mie–Grüneisen type equation of state (EOS)

$$\rho e = f(\rho) p + g(\rho) \tag{12}$$

is used for gas, where ρ is the fluid density, e is the total energy per unit mass of the fluid, p is the fluid pressure, $f(\rho)$ and $g(\rho)$ are functions of fluid density. For example, for the ideal gas

$$f(\rho) = \frac{1}{\gamma - 1}, \ g(\rho) = 0.0$$

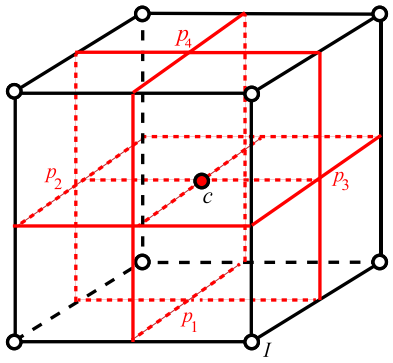

Fig. 1. The spatial discretization of staggered grid.

while for the products of high explosive

$$f(\rho) = \frac{1}{\omega}, \qquad g(\rho) = -\frac{A}{\omega}\left(1 - \frac{\omega\rho}{R_1\rho_0}\right)\exp\left(-\frac{R_1\rho_0}{\rho}\right) - \frac{B}{\omega}\left(1 - \frac{\omega\rho}{R_2\rho_0}\right)\exp\left(-\frac{R_2\rho_0}{\rho}\right) \tag{13}$$

where A, B, R_1, R_2 and ω are the parameters of JWL EOS, ρ_0 is the initial density.

The weak incompressible EOS is adopted for water where the fluid pressure is calculated by

$$p = c_0^2(\rho - \rho_0) + p_0 \tag{14}$$

where c_0 is the artificial sound speed and p_0 is the initial pressure.

The stress-rate of solid is updated with the strain-rate by a constitutive equation as

$$\sigma_{ij}^{\nabla} = \sigma_{ij}^{\nabla}(\dot{\epsilon}_{ij}, \sigma_{ij}, \text{etc.}) \tag{15}$$

where

$$\sigma_{ij}^{\nabla} = \dot{\sigma}_{ij} - \sigma_{ik}\Omega_{jk} - \sigma_{jk}\Omega_{ik} \tag{16}$$

is the Jaumann rate of the Cauchy stress tensor,

$$\Omega_{ij} = (\dot{u}_{i,j} - \dot{u}_{j,i})/2 \tag{17}$$

is the spin tensor.

3. The multi-material arbitrary Lagrangian Eulerian method

The MMALE method adopts a hybrid Lagrangian and Eulerian description of indirect ALE which consists of a Lagrangian phase and a Euler phase.

3.1. Lagrangian phase

In the Lagrangian phase, each 3D cell c is divided into eight subcells as illustrated in Fig. 1.

The mass of the subcell s_{cI} related to corner node I is calculated as

$$m_{cI} = \rho_c V_{cI} \tag{18}$$

where ρ_c is the density of the cell and V_{cI} is the volume of the subcell s_{cI}. The cell mass m_c and nodal mass m_I are obtained by summing up the related mass of the subcells as

$$m_c = \sum_I m_{cI}, \quad m_I = \sum_c m_{cI} \tag{19}$$

The internal force of the node I is calculated as

$$f_{iI} = \sum_c f_{icI} = -\sum_c P_c \int_{\Gamma_{cI}} n_i d\Gamma + \sum_c f_{icI\text{Vis}} + \sum_c f_{icI\text{HG}} \tag{20}$$

where f_{icI} is the corner force of the subcell s_{cI}, P_c denotes the pressure of cell c, Γ_{cI} denotes the inner boundary surfaces of subcell s_{cI} and n_i denotes the normal vector, $f_{icI\text{Vis}}$ includes the fluid viscous force and artificial viscous force [51,52] applied to provide the entropy production and introduce dissipation for shock discontinuity, $f_{icI\text{HG}}$ is the hourglass viscosity force [53] added to eliminate the hourglass modes. As the cell pressure, energy and density are stored in the cell center of MMALE grid, the computation of

nodal mass and forces are essentially realized with the one-point Gaussian quadrature. By means of Lagrangian subzonal masses and pressures [53,54], the hourglass distortion can be eliminated.

The external force of node I is obtained as

$$\tilde{f}_{iI} = m_I b_{iI} + \int_{\Gamma_{tI}} \bar{t}_i \mathrm{d}\Gamma$$

where Γ_{tI} denotes the force boundary in the support domain of the node I.

The predictor–corrector scheme [55] is adopted for the time integration of MMALE. In the predictor step, the nodal coordinates of the MMALE grid are updated to the half-step $n+1/2$ according to the nodal velocity v_{iI}^n as

$$x_{iI}^{n+1/2} = x_{iI}^n + \frac{1}{2} v_{iI}^n \Delta t \tag{21}$$

Then the cell volume $V_c^{k+1/2}$ is calculated by the positions of nodes at the half-step $n+1/2$ and the new pressure $P_c^{n+1/2}$ is calculated based on the isentropic hypothesis as

$$P_c^{n+1/2} = P_c^n - \rho_c^n (\kappa_c^n)^2 \frac{V_c^{n+1/2} - V_c^n}{V_c^n} \tag{22}$$

where κ denotes the adiabatic sound velocity calculated by the EOS.

The nodal force $f_{iI}^{n+1/2}$ at the half-step $n+1/2$ is obtained by substituting the temporary pressure $P_c^{n+1/2}$ into Eq. (20) as

$$f_{iI}^{n+1/2} = \sum_c f_{icI}^{n+1/2} = -\sum_c P_c^{n+1/2} \int_{\Gamma_{cI}} n_i d\Gamma + \sum_c f_{icI\mathrm{Vis}}^{n+1/2} + \sum_c f_{icI\mathrm{HG}}^{n+1/2} \tag{23}$$

Then the nodal velocities and positions are updated in the corrector step by Eq. (8) as

$$v_{iI}^{n+1} = v_{iI}^n + \frac{f_{iI}^{n+1/2} + \tilde{f}_{iI}^{n+1/2}}{m_I} \Delta t \tag{24}$$

$$v_{iI}^{n+1/2} = \frac{1}{2}(v_{iI}^n + v_{iI}^{n+1}) \tag{25}$$

$$x_{iI}^{n+1} = x_{iI}^n + v_{iI}^{n+1/2} \Delta t \tag{26}$$

The new cell volume V_c^{n+1} is obtained by the nodal position x_{iI}^{n+1} and the density is updated as $\rho_c^{n+1} = m_c / V_c^{n+1}$. The compatible discretization is adopted to preserve the energy conservation of the whole system [56] where the specific internal energy of cell c is calculated by

$$E_c^{n+1} = E_c^n + \frac{-\sum_I f_{icI}^{n+1/2} v_{iI}^{n+1/2}}{m_c} \Delta t \tag{27}$$

The new cell pressure P_c^{n+1} is updated by the adopted EOS of the fluid as $P_c^{n+1} = P(\rho_c^{n+1}, E_c^{n+1})$. For the multi-material cells which contain multiple materials in the MMALE method, the cell pressure P_l of each material l calculated by different EOS is not equal. Thus a closure model [57–59] is needed to derive a multi-material cell pressure for the calculation of the nodal force in Eq. (20) and to determine different material volume fraction. The Tipton pressure relaxation model [59] is the most popular one and used in this paper. Additionally, the material centroid ξ_{il} is updated based on the constant parametric coordinate method [60] in the Lagrangian phase for the material interface reconstruction.

3.2. Euler phase

Mesh quality inspection is conducted after each Lagrangian phase to determine whether the grid needs rezoning. The cell shape [61] and the average nodal displacement between two Lagrangian steps [62] can be used to judge whether the grid is distorted. The rezoning and remapping phases are not conducted until the grid is determined distorted after several Lagrangian steps.

In the rezoning phase, the quality of the computational grid is improved. The rezoned mesh is required to conform the material interface in traditional ALE method, which is difficult and time-consuming. However, the MMALE method allows the material interface pass through the cell and thus the rezoning phase is not affected by the location of the material interface. Therefore any mesh rezoning methods [61,63] can be adopted to improve the distorted grid.

The accurate polyhedron intersection based method [38,49] is adopted for its accuracy in multi-phase remapping which includes three steps: the reconstruction of multi-phase interface, linear reconstruction of physical field, polyhedron subdivision and intersection as illustrated in Fig. 2. The MoF method can be used to reconstruct the clear material surface in MMALE cells of the old grid with the volume fraction and centroids of different materials, as shown in Fig. 2(a), which is proved robust and accurate in multiphase flow situations such as bubbles, cavitation and explosion [36,49,64–68]. Then the old cells are subdivided into single-material polyhedrons by the planar material surface as shown in Fig. 2(b) by the white line. Through the modified “clipping and capping” algorithm [38], various situations of polyhedron subdivision including convex subdivision, non-convex subdivision and multiple subdivision can be handled well. Finally the physical variables of the new grid are accumulated from its intersection fragments with single-material polyhedrons of the old grid, as illustrated in Fig. 2(c).

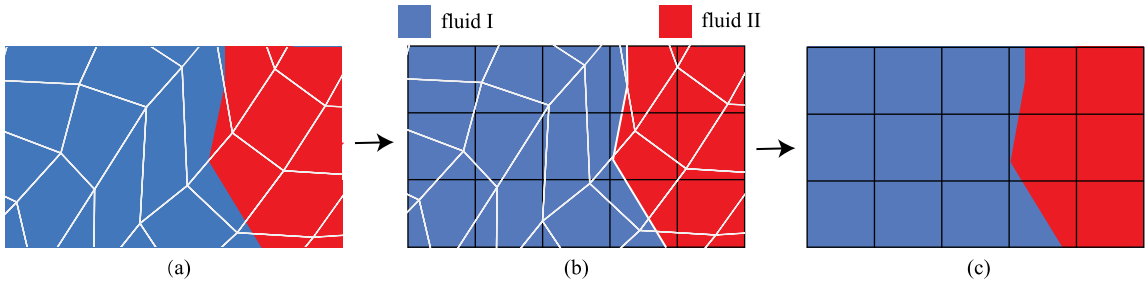

Fig. 2. Remapping process of MMALE. (a) the old MMALE grid in white with multi-phase interface reconstructed, (b) the old grid cut into polyhedrons of pure material and intersected with the new grid in black, (c) physical variables of the new grid obtained from the intersection pieces.

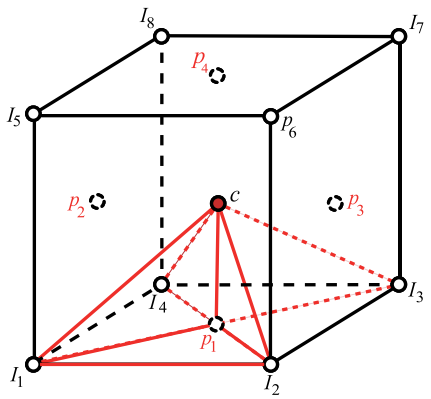

Fig. 3. Division of a hexahedral cell with nodes, surface centers and nodes [38].

For state variables stored in the cell centers, each cell of the new grid is divided into 24 tetrahedrons such as tetrahedron ($I_1 I_2 p_1 c$) with cell center, surface centers and nodes as shown in Fig. 3. All the tetrahedrons intersect with the polyhedrons of old cells and the physical variables of each new cell are obtained by summing its related intersection fragments. With the "clipping and projecting" method [38], the intersection fragments inside the control volume of each new cell can be acquired precisely.

For example, the volume, mass and internal energy of the kth material in the new cell are obtained by summing the intersection fragments in the control volume Ω_c as

$$V_{kc} = \sum_p V\left(\mathscr{H}_{pkc}\right) \tag{28}$$

$$m_{kc} = \sum_p m\left(\mathscr{H}_{pkc}\right) \tag{29}$$

$$E_{kc} = \sum_p E\left(\mathscr{H}_{pkc}\right) \tag{30}$$

where $\mathscr{H}_{pkc} = \Omega_c \cap Q_{pk}$ denotes the intersection part of Ω_c with the kth material polyhedron Q_{pk} in pth cell of the old grid. Then the total volume, mass and internal energy of the cell c are obtained as

$$V_c = \sum_k V_{kc} \tag{31}$$

$$m_c = \sum_k m_{kc} \tag{32}$$

$$E_c = \sum_k E_{kc} \tag{33}$$

The kinematics and kinetics variables are stored on the nodes and need special handling. Tetrahedrons are divided from the control volume Ω_I of new grid node and are intersected with the single-material polyhedrons. The mass and momentum of the kth material stored on the node I are calculated by summing the intersection fragments in the nodal control volume Ω_I as

$$m_{kI} = \sum_p m\left(\mathscr{H}_{pkI}\right) \tag{34}$$

$$M_{ikI} = \sum_p M_i\left(\mathscr{H}_{pkI}\right) \tag{35}$$

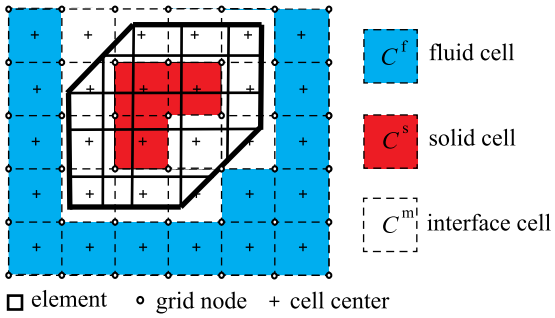

Fig. 4. The spatial discretization of the IALEFEM.

where $\mathscr{H}_{pkI} = \Omega_I \cap Q_{pk}$ denotes the intersection part of Ω_I with the single-material polyhedron Q_{pk}.

Then the total momentum stored on the node I is obtained as

$$m_I = \sum_k m_{kI} \tag{36}$$

$$M_{iI} = \sum_k M_{ikI} \tag{37}$$

Subsequently, the nodal velocity in the new grid is calculated as

$$v_{iI} = \frac{M_{iI}}{m_I} \tag{38}$$

After these two steps, the variables have been remapped to the newly rezoned grid from the old grid and another round of Lagrangian phase would continue.

4. The immersed MMALE finite element method

This section introduces the immersed multi-material arbitrary Lagrangian-Eulerian finite element method (IALEFEM) in which the FEM is strongly coupled with the MMALE method to simulate FSI problems and the fluid–structure-interaction is realized through the MMALE grid. Similar to the MMALE, the IALEFEM also consists of a Lagrangian phase and a Euler phase.

4.1. Spatial discretization

The FEM solves the Lagrangian momentum equation and shares the same calculation framework as the Lagrangian phase of MMALE. With the concept of the immersed boundary method [69], the FEM elements which discretize the solid structures are immersed in the MMALE grid and track the FSI interface implicitly. The fluid occupies the whole MMALE grid and the computational domain occupied by the solid elements are filled with virtual fluid. As shown in Fig. 4, cells without any FEM element node are classified as fluid cells while cells containing FEM element node are classified as interface or solid cells depending on whether there is a fluid cell in their 26 surrounding cells. Finite elements such as hexahedron, tetrahedron, solid shell elements and other elements can all be applied here to discretize the solid region and hexahedral elements are mainly adopted in this article.

Therefore, the density, stress and internal energy in the computational domain can be expressed as

$$\rho = \rho^{\mathrm{f}} + \mu(\rho^{\mathrm{s}} - \rho^{\mathrm{f}}) \tag{39}$$

$$\sigma_{ij} = \sigma_{ij}^{\mathrm{f}} + \mu(\sigma_{ij}^{\mathrm{s}} - \sigma_{ij}^{\mathrm{f}}) \tag{40}$$

$$e = e^{\mathrm{f}} + \mu(e^{\mathrm{s}} - e^{\mathrm{f}}) \tag{41}$$

where the superscripts f and s denote the variables associated with fluid and solid, respectively,

$$\mu(\boldsymbol{x}) = \begin{cases} 0 & \boldsymbol{x} \in \Omega^{\mathrm{f}} \\ 1 & \boldsymbol{x} \in \Omega^{\mathrm{s}} \end{cases} \tag{42}$$

with Ω^{f} denoting the fluid region and Ω^{s} the solid region. As indicated by Eqs. (39)~(41), the physical variables of the whole computational domain can be obtained by integrating the fluid domain (including the virtual fluid) in MMALE cells and then adding the solid modification part (subtracting the virtual fluid) from solid elements.

Integrating the first term on the right-hand side of Eq. (39) over the fluid domain leads to Eqs. (18)~(20) by the cell-centered quadrature of MMALE. For the second term on the right-hand side of Eq. (39), substituting $\rho = \mu(\rho^{\mathrm{s}} - \rho^{\mathrm{f}})$ into Eq. (9) and integrating over the solid domain Ω^{s} lead to the nodal mass of finite elements subtracting the virtual fluid mass

$$m_J = \int_{\Omega^{\mathrm{s}}} \left(\rho^{\mathrm{s}} - \rho^{\mathrm{f}}\right) N_J \mathrm{d}\Omega = \sum_e \left(\rho_e - \rho_e'\right) V_e N_{Je} \tag{43}$$

where ρ'_e denotes the density of the virtual fluid in the support domain of element e, V_e is the volume of element e and N_{Je} is the shape function of node J at the center of element e.

Similar to the nodal mass, the internal nodal force of FEM grid subtracting the part of virtual fluid can be derived by substituting $\sigma_{ij} = \mu(\sigma^{\mathrm{s}}_{ij} - \sigma^{\mathrm{f}}_{ij})$ into Eq. (10) and integrating over the solid domain, namely,

$$f_{iJ} = \int_{\Omega^{\mathrm{s}}} \left(\sigma^{\mathrm{s}}_{ij} - \sigma^{\mathrm{f}}_{ij}\right) N_{J,j}\mathrm{d}\Omega + f_{iI\mathrm{FB}} = -\sum_e V_e N_{Je,j}\left(\sigma_{ije} + P'_e\delta_{ij}\right) + f_{iI\mathrm{FB}} \tag{44}$$

where σ_{ije} denotes the stress of element e and P'_e denotes the pressure of the virtual fluid which is located in the support domain of element e. As the one-point Gaussian quadrature is used in this article, the Flanagan/Belytschko damping force [70] $f_{iI\mathrm{FB}}$ is employed to suppress the hourglass modes. The external nodal force is calculated as

$$\tilde{f}_{iJ} = \int_{\Omega^{\mathrm{s}}} N_J \rho^{\mathrm{s}} b_i d\Omega + \int_{\Gamma^{\mathrm{s}}_t} N_J \bar{t}_i \mathrm{d}\Gamma \tag{45}$$

where Γ^{s}_t denotes the traction boundary of the material domain Ω^{s}.

The Lagrangian momentum equation is solved on the MMALE grid and thus the nodal mass and forces of the immersed FEM elements are mapped to the MMALE grid. The total mass and forces of the MMALE grid are obtained as

$$m_I = \sum_c \rho_c V_{cI} + \sum_J m_J N_{IJ} \tag{46}$$

$$f_{iI} = \sum_c f_{icI} + \sum_J f_{iJ} N_{IJ} \tag{47}$$

where N_{IJ} is the shape function of node I at the element node J and f_{icI} contains the viscous force and the hourglass viscosity forces applied in the MMALE. The same technique such as the closure model for multi-phase cells are also adopted for accurate and robust fluid computation. With Eqs. (46) and (47), the MMALE grid nodes located far from the FEM elements represent the movement of the fluid while the grid nodes within the elements represent the movement of solid. For interface cells of MMALE grid, the grid nodes are both influenced by solid and fluid and they represent the weighted average movement of fluid and solid with the weight N_{IJ}.

4.2. Lagrangian phase

The predictor–corrector scheme is also adopted for time integration of IALEFEM to keep consistent with that of MMALE. For the predictor step, a temporary MMALE grid is updated with Eq. (21) and the position of a FEM node at the half-step $n + 1/2$ is interpolated from the temporary MMALE grid as

$$x^{n+1/2}_{iJ} = \sum_{I=1}^{8} x^{n+1/2}_{iI} N_{IJ} \tag{48}$$

Then the volume of the solid elements at $n + 1/2$ are predicted by

$$V^{n+1/2}_e = V(x^{n+1/2}_{iJ}) \tag{49}$$

The temporary stress at the half-step $n + 1/2$ is calculated by the constitutive model as $\sigma^{n+1/2}_{ije} = \sigma_{ij}\left(\sigma^n_{ije}, \dot{\varepsilon}^n_{ije}, \dot{\Omega}^n_{ije}\right)$ where the strain rate and vorticity rate of the Gauss point are calculated with nodal velocities of FEM as

$$\dot{\varepsilon}^n_{ije} = \sum_{J=1}^{8} \frac{1}{2}(N_{J,j} v^n_{iJ} + N_{J,i} v^n_{jJ}) \tag{50}$$

$$\dot{\Omega}^n_{ije} = \sum_{J=1}^{8} \frac{1}{2}(N_{J,j} v^n_{iJ} - N_{J,i} v^n_{jJ}) \tag{51}$$

The internal nodal force of the FEM node is updated with the one-point Gauss quadrature as

$$f^{n+1/2}_{iJ} = -\sum_e V^{n+1/2}_e N_{Je,j}\left(\sigma^{n+1/2}_{ije} + P'^{n+1/2}_e \delta_{ij}\right) + f^{n+1/2}_{iI\mathrm{FB}} \tag{52}$$

where the temporary pressure $P'^{n+1/2}_e$ of the fluid is calculated by the isentropic hypothesis as $P^{n+1/2}_c$ in Eq. (22).

Substituting the internal nodal force $f^{n+1/2}_{iJ}$ and $f^{n+1/2}_{icI}$ calculated by Eq. (23) into Eq. (47) gives the nodal force as

$$f^{n+1/2}_{iI} = \sum_c f^{n+1/2}_{icI} + \sum_J f^{n+1/2}_{iJ} N_{IJ} \tag{53}$$

Then the nodal acceleration is obtained by substituting m_I and $f^{n+1/2}_{iI}$ into Eq. (8) and updating the momentum equation.

For the corrector step, the nodal velocities and positions of the MMALE grid are updated to the next step with Eqs. (24)~(26) and then the state variables of the fluid cells and solid elements are updated with respective ways of MMALE and FEM. For solid

elements, the nodal velocities and displacements are updated by interpolating the MMALE grid nodal velocities and displacements as

$$v_{iJ}^{n+1} = \sum_{I=1}^{8} v_{iI}^{n+1} N_{IJ} \tag{54}$$

$$x_{iJ}^{n+1} = \sum_{I=1}^{8} x_{iI}^{n+1} N_{IJ} \tag{55}$$

$$v_{iJ}^{n+1/2} = \sum_{I=1}^{8} v_{iI}^{n+1/2} N_{IJ} \tag{56}$$

The strain rate and vorticity rate of the solid elements are calculated with the updated FEM nodal velocities as

$$\dot{\varepsilon}_{ije}^{n+1/2} = \sum_{I=1}^{8} \frac{1}{2}(N_{J,j} v_{iJ}^{n+1/2} + N_{J,i} v_{jJ}^{n+1/2}) \tag{57}$$

$$\dot{\Omega}_{ije}^{n+1/2} = \sum_{I=1}^{8} \frac{1}{2}(N_{J,j} v_{iJ}^{n+1/2} - N_{J,i} v_{jJ}^{n+1/2}) \tag{58}$$

Then the stress is updated by the constitutive equation as $\sigma_{ije}^{n+1} = \sigma_{ij}\left(\sigma_{ijp}^{n}, \dot{\varepsilon}_{ije}^{n+1/2}, \dot{\Omega}_{ije}^{n+1/2}\right)$ and the density is obtained by $\rho_{ije}^{n+1} = m_e / V_e^{n+1}$. For the fluid cells, the internal energy is updated according to the energy conservation law and then the pressure is updated by the EOS. Substituting Eq. (41) into Eq. (1), we obtain

$$\rho \frac{\mathrm{d}e}{\mathrm{d}t} = \rho^{\mathrm{f}} \frac{\mathrm{d}e^{\mathrm{f}}}{\mathrm{d}t} + \mu\left(\rho^{\mathrm{s}} \frac{\mathrm{d}e^{\mathrm{s}}}{\mathrm{d}t} - \rho^{\mathrm{f}} \frac{\mathrm{d}e^{\mathrm{f}}}{\mathrm{d}t}\right) = \dot{\varepsilon}_{ij}(\sigma_{ij}^{\mathrm{f}} + \mu(\sigma_{ij}^{\mathrm{s}} - \sigma_{ij}^{\mathrm{f}})) \tag{59}$$

Integrating Eq. (59) with cell center quadrature for fluid and Gauss quadrature for solid leads to

$$\sum_c \left(m_c - \sum_e \rho_e' V_{ce}\right) \frac{\mathrm{d}E_c}{\mathrm{d}t} + \sum_e \rho_e V_e \frac{\mathrm{d}E_e}{\mathrm{d}t} = -\sum_c \sum_I v_{iI} f_{icI} + \sum_e \dot{\varepsilon}_{ije} \sigma_{ije} V_e + \sum_e \dot{\varepsilon}_{iie} P_e' V_e \tag{60}$$

where E_e is the specific internal energy of solid element e, E_c is the specific internal energy of cell c in the MMALE grid and V_{ce} is the common volume of the solid element e and cell c.

The energy conservation equation is satisfied on the solid elements, i.e.

$$\rho_e \frac{\mathrm{d}E_e}{\mathrm{d}t} = \dot{\varepsilon}_{ije} \sigma_{ije} \tag{61}$$

so that Eq. (60) can be rewritten as

$$\sum_c \left(m_c - \sum_e \rho_e' V_{ce}\right) \frac{\mathrm{d}E_c}{\mathrm{d}t} = -\sum_c \sum_I v_{iI} f_{icI} + \sum_c \sum_e \dot{\varepsilon}_{iie} P_e' V_{ce} \tag{62}$$

where the V_{ce} represents the intersection volume of cell c and element e and the right-hand side of Eq. (62) is used to update the internal energy of the real fluid.

For pure fluid cells without solid elements, $V_{ce} = 0$ and Eq. (62) changes into $\sum_c m_c \frac{\mathrm{d}E_c}{\mathrm{d}t} = -\sum_c \sum_I v_{iI} f_{icI}$ which is the same as Eq. (27). For solid cells filled with virtual fluid, the left-hand side of Eq. (62) may equal to zero when $m_c - \sum_e \rho_e' V_{ce} = 0$ but the right-hand side of Eq. (62) may not, which will cause computational instability. In fact, as the calculation is not affected by the virtual fluid in solid cells, Eq. (27) can also be adopted for updating the virtual fluid energy. For interface cells with both real fluid and solid, the internal energy E_c of cell c should be updated with Eq. (62) for the real fluid. However, as the volume changes and $\dot{\varepsilon}_{iie}$ of the solid are always much lower compared with those of the fluid (especially when the solid is rigid or the fluid is gas, etc.), the second term of RHS is always quite small compared with the first term of RHS and the cell energy can be approximately and efficiently updated with Eq. (27).

By immersing the FEM elements in the MMALE grid and assembling the nodal force and momentum of the MMALE grid from both the solid and fluid, the strong FSI coupling is realized in the IALEFEM. Fluid and solid are in the same velocity field with the no-slip interaction and their movement is represented by the nodal velocities and positions of the MMALE and FEM grids. The displacement continuity condition of FSI in all directions is also automatically satisfied. In the Lagrangian phase, the Lagrangian solid elements move in accordance with the MMALE grid and therefore the natural coordinates of FEM nodes in each cell keep unchanged before the rezoning phase.

Compared to the IALEMPM [49], the IALEFEM is more accurate for the FSI problems with small and moderate solid deformation. The IALEMPM suffers from the spurious strain induced by the mixed FSI velocity field on the MMALE grid and thus needs to reproduce a virtual solid grid to update the strain and stress. However in IALEFEM, only the nodal velocity of FEM element is updated from the MMALE grid and represents the actual movement of solid. The solid strain and stress are calculated with the FEM nodal velocities and are not influenced by the mixed FSI nodal velocity. Meanwhile the cell crossing noise of MPM caused by the gradient of the piecewise linear shape function is also eliminated as the solid strain and stress are obtained with the Gauss quadrature of FEM elements.

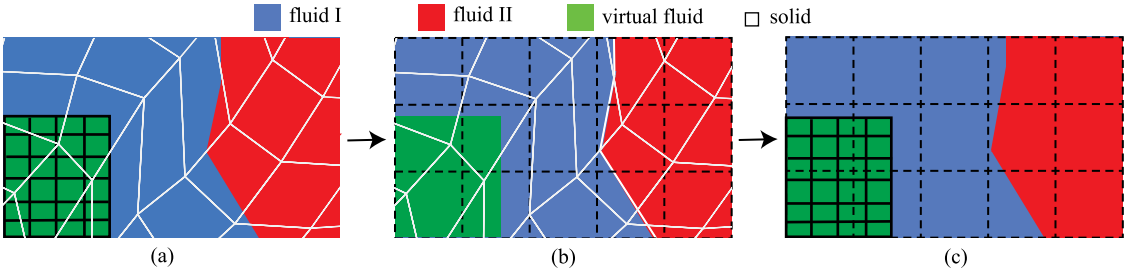

Fig. 5. Remapping process of IALEFEM. (a) the computational domain including the Lagrangian FEM elements and old MMALE grid with multi-phase interface reconstructed, (b) the fluid domain including the real fluid and virtual fluid covered by elements are remapped to the new grid, (c) the computational domain including the Lagrangian FEM elements and new MMALE grid modified by solid variables.

4.3. Euler phase

The maximum ratio of side lengths and largest inclined angle related to the cell shape are monitored to judge whether the grid needs rezoning and remapping phase. As the computational grid of IALEFEM is not required to conform the material interface or the interface of fluid and solid, any rezoning method can be used here according to the practical demand. We rezone the distorted grid to a 3D structured orthogonal grid, which is convenient and makes it easy to determine the natural coordinates of solid elements in MMALE cells.

For the remapping phase of IALEFEM, the physical variables in the newly created domain is obtained from the old computational domain including both the old grid and FEM elements. The process of the remapping phase of IALEFEM is illustrated in Fig. 5 which includes two steps: remapping of the fluid region with the accurate polyhedron intersection based method [38,49] and physical variables correction with solid elements. During the first step, the multi-phase interface and linear physical field are reconstructed in the old grid (Fig. 5(a)) and then the physical variables of the fluid (including the real fluid and virtual fluid) are obtained as the way in MMALE (Fig. 5(b)). The cell-centered variables are calculated by accumulating in Eqs. (28)~(33) while the kinematics and kinetics variables are calculated by Eqs. (34)~(38). Finally the new grid is modified by the solid region in the second step as illustrated in Fig. 5(c).

New natural coordinate of each FEM node is calculated to obtain the shape function N_{IJ} in the new grid and modification is applied on the nodal mass and momentum as

$$m_I = \sum_k \sum_p m\left(\mathscr{H}_{pkI}\right) + \sum_J m_J N_{IJ} \tag{63}$$

$$M_{iI} = \sum_k \sum_p M_i\left(\mathscr{H}_{pkI}\right) + \sum_J m_J v_{iJ} N_{IJ} \tag{64}$$

The final velocity of the new grid can be calculated by Eq. (38). The nodal mass m_I calculated by intersection is adopted to calculate the nodal velocity and then the constant nodal mass used in the Lagrangian phase is calculated by Eq. (46). After these two steps, the physical variables have been remapped to the newly rezoned grid from the old domain and next Lagrangian phase would continue. As the Euler phase is time-consuming with the accurate polyhedron intersection based method [38,49] and the intersection process of each new cell with the old grid is mutually independent, the multi-threading OpenMP parallel implementation of cell intersection process is applied in the Euler step to enhance the computational efficiency of IALEFEM. In both MMALE and IALEFEM, the Euler phase only carries out when the grid is distorted, so that there are many Lagrangian steps between two Euler phases. The solution scheme of IALEFEM is briefly illustrated in Fig. 6.

Compared with the coupled MMALE-FEM presented by Chen et al. [39], the FEM elements can be overlapped with the MMALE grid which makes the rezoning phase of IALEFEM not restricted by the solid surface. Thus the efficiency of the Euler phase is enhanced significantly and the robustness is strengthened in dealing with large deformation and movement of solid structures.

4.4. Slip fluid–structure interaction

The no-slip interaction of fluid and solid in IALEFEM imposes an additional restriction on the tangential velocity of inviscid fluid and applies extra tangential force for solids. As the velocity gradient will not cause tangential force in the inviscid fluid such as air, the restriction on the tangential velocity will only be restricted in one layer of fluid cells nearest the fluid–solid interface which makes the no-slip interaction a valid approximation [49]. However, when fluid and solid have close density and significantly different velocities (such as the water-entry problems), the tangential force applied to the solid is non-negligible with the no-slip fluid–structure interaction. Therefore a slip fluid–structure-interaction method of IALEFEM should be established here.

Integrating over the real fluid region, the nodal mass and force of the real fluid are obtained by removing the solid part from Eqs. (46) and (47) as

$$m_I^{\mathrm{f}} = \sum_c \rho_c V_{cI} + \sum_J m'_J N_{IJ} \tag{65}$$

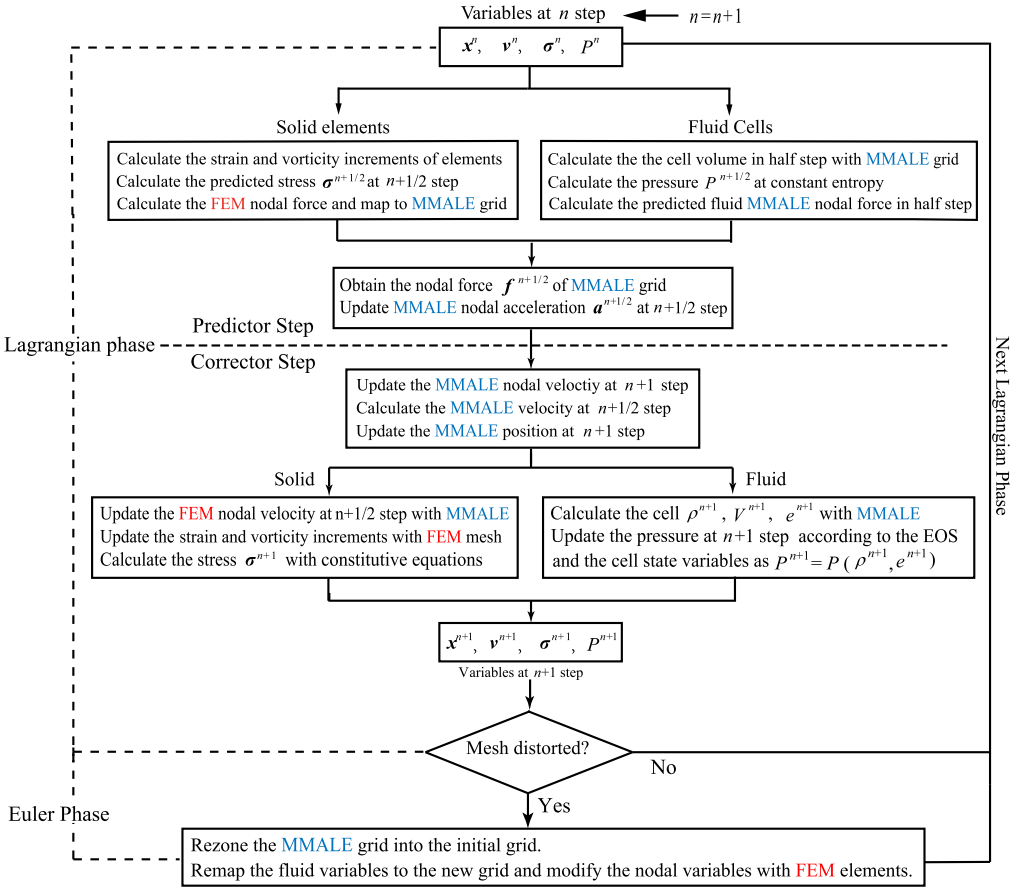

Fig. 6. Flowchart of the IALEFEM.

$$f_{iI}^{\mathrm{f}} = \sum_{c} f_{icI} + \sum_{J} f'_{iJ} N_{IJ} \tag{66}$$

where $m'_J = -\sum_e \rho'_e V_e N_{Je}$ and $f'_{iJ} = -\sum_e V_e N_{Je,j}(P'_e \delta_{ij})$ denote the nodal mass and nodal force of the virtual fluid calculated with the one point Gauss quadrature. Meanwhile the nodal mass and force of the solid region can be obtained as

$$m_I^{\mathrm{s}} = \sum_{J} m_J^{\mathrm{s}} N_{IJ} \tag{67}$$

$$f_{iI}^{\mathrm{s}} = \sum_{J} f_{iJ}^{\mathrm{s}} N_{IJ} \tag{68}$$

where $m_J^{\mathrm{s}} = \sum_e \rho_e V_e N_{Je}$ and $f_{iJ}^{\mathrm{s}} = -\sum_e V_e N_{Je,j}\sigma_{ije} + f_{i\mathrm{IFB}}$ denote the nodal mass and nodal force of the solid calculated with the one point Gauss quadrature.

The fluid–structure-interaction of IALEFEM is implemented by assembling the nodal mass and forces on the MMALE grid. For pure solid and fluid cells in the computational domain, contributions to the nodal physical variables come from either solid or fluid. Therefore the slip fluid–structure-interaction should be realized on nodes of the interface cells.

The nodes of interface cells are firstly classified by the cell type of surrounding cells as illustrated in Fig. 7. The cell nodes are defined as no-slip nodes when all of the surrounding cells are solid or interface cells, which means the node is located in the solid region. The other nodes are slip nodes as they are located in the fluid region and should move with the fluid flow.

Substituting Eqs. (65) and (66) into Eq. (8) leads to

$$\dot{v}_{iI}^{\mathrm{f}} = \frac{f_{iI}^{\mathrm{f}} + \tilde{f}_{iI}^{\mathrm{f}}}{m_I^{\mathrm{f}}} \tag{69}$$

where $\tilde{f}_{iI}^{\mathrm{f}}$ is the external force of the fluid including the contact force of fluid–structure-interaction.

Substituting Eqs. (67) and (68) into Eq. (8) leads to

$$\dot{v}_{iI}^{\mathrm{s}} = \frac{f_{iI}^{\mathrm{s}} + \tilde{f}_{iI}^{\mathrm{s}}}{m_I^{\mathrm{s}}} \tag{70}$$

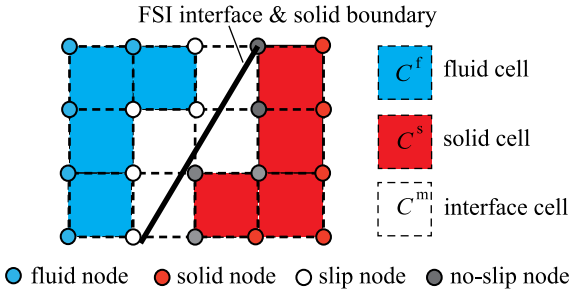

Fig. 7. Classification of cell nodes for slip fluid–structure-interaction method.

where $\tilde{f}_{iI}^{\mathrm{s}}$ is the external force of the solid including the contact force of fluid–structure-interaction.

Irrespective of the FSI contact force, the predicted nodal velocities of solid and fluid can be updated on the MMALE grid as

$$v_{iI}^{\mathrm{f},n+1} = v_{iI}^{\mathrm{f},n} + \dot{v}_{iI}^{\mathrm{f},n+1/2}\Delta t \tag{71}$$

$$v_{iI}^{\mathrm{s},n+1} = v_{iI}^{\mathrm{s},n} + \dot{v}_{iI}^{\mathrm{s},n+1/2}\Delta t \tag{72}$$

where $v_{iI}^{\mathrm{f},n}$ and $v_{iI}^{\mathrm{s},n}$ are the fluid and solid nodal velocity at time step n. The fluid velocity $v_{iI}^{\mathrm{f},n}$ equals to the nodal velocity on the MMALE grid while the solid velocity $v_{iI}^{\mathrm{s},n}$ of the MMALE grid can be calculated by remapping mass and momentum from FEM nodes as

$$v_{iI}^{\mathrm{s},n} = \frac{M_{iI}^{\mathrm{s},n}}{m_I^{\mathrm{s},n}} = \frac{\sum_J v_{iJ}^n m_J N_{IJ}}{\sum_J m_J N_{IJ}}$$

The displacement continuity condition of FSI in the normal directions of the solid should be satisfied and the tangential velocity is not restricted. With the submerged FEM elements, the normal direction of the solid is determined as

$$\eta_{iI} = \frac{\sum_J \eta_{iJ} m_J N_{IJ}}{\sum_J m_J N_{IJ}}$$

where η_{iJ} is the normal direction of element node J determined by identifying the outer surface of FEM [71] and calculating with the coordinates of surface nodes. Therefore the tangential nodal velocities of fluid and solid on the interface cells are obtained as

$$v_{iI\tan}^{\mathrm{f},n+1} = v_{iI}^{\mathrm{f},n+1} - v_{iI}^{\mathrm{f},n+1}\eta_{iI} \tag{73}$$

$$v_{iI\tan}^{\mathrm{s},n+1} = v_{iI}^{\mathrm{s},n+1} - v_{iI}^{\mathrm{s},n+1}\eta_{iI} \tag{74}$$

The nodal velocity in the normal direction is calculated as

$$v_{iI\mathrm{nor}}^{n+1} = \frac{m_I^{\mathrm{f}} v_{iI}^{\mathrm{f},n+1}\eta_{iI} + m_I^{\mathrm{s}} v_{iI}^{\mathrm{s},n+1}\eta_{iI}}{m_I^{\mathrm{f}} + m_I^{\mathrm{s}}} \tag{75}$$

and the actual nodal velocities of fluid and solid are updated as

$$v_{iI\mathrm{Real}}^{\mathrm{f},n+1} = v_{iI\mathrm{nor}}^{n+1} + v_{iI\tan}^{\mathrm{f},n+1} \tag{76}$$

$$v_{iI\mathrm{Real}}^{\mathrm{s},n+1} = v_{iI\mathrm{nor}}^{n+1} + v_{iI\tan}^{\mathrm{s},n+1} \tag{77}$$

In this way, the slip fluid–structure-interaction is realized on the fluid and solid simultaneously as illustrated in Fig. 8. Then the MMALE grid is updated with the fluid velocity $v_{iI\mathrm{Real}}^{\mathrm{f},n+1}$ to calculate the physical variables of fluid and a virtual solid grid is obtained with the solid velocity $v_{iI\mathrm{Real}}^{\mathrm{s},n+1}$ to update the physical variables of the solid.

However, as the solid and fluid are not in the same displacement and velocity field with different nodal velocities, the solid elements need to be re-located in the MMALE grid with updated natural coordinates. The re-location of the elements is conducted in the surrounding cells and determination of new natural coordinates includes the estimation of initial values and an iterative process. Meanwhile Eq. (65) may approach or less than zero for some interface cells, which will cause computational instability in Eq. (69).

Therefore another slip FSI method is presented and adopted in this article which updates only the solid nodal velocities with the calculated FSI force and then uses the solid velocity field to serve as the velocity boundary for fluid. The MMALE grid are also updated with the solid nodal velocities, namely,

$$v_{iI}^{n+1} = v_{iI\mathrm{Real}}^{\mathrm{f},n+1} = v_{iI\mathrm{Real}}^{\mathrm{s},n+1} \tag{78}$$

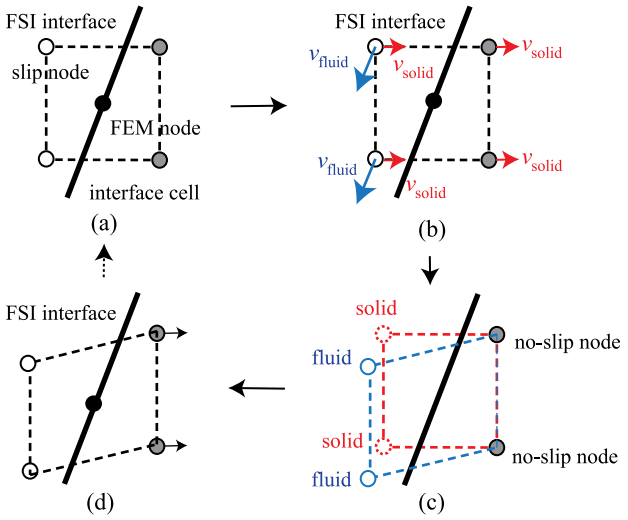

Fig. 8. Diagram of the slip fluid–structure-interaction method in IALEFEM (a) the initial interface cell with slip nodes and no-slip nodes (b) the interface cell with nodal velocities of fluid and solid calculated (c) the interface cell updated with nodal velocities of fluid and solid (d) the interface cell updated with the FEM node re-located.

In this way, the solid and fluid are still in the same displacement and velocity field and the solid nodal velocity $v_{iI}^{\mathrm{s},n}$ can be directly substituted by $v_{iI}^{\mathrm{s},n} = v_{iI}^{\mathrm{f},n} = v_{iI}^{n}$. Substituting Eqs. (71) and (72) into Eq. (75) leads to

$$v_{iI\mathrm{nor}}^{n+1} = \frac{m_I^{\mathrm{f}}(v_{iI}^{\mathrm{f},n} + \dot{v}_{iI}^{\mathrm{f},n+1/2}\Delta t)n_{iI} + m_I^{\mathrm{s}}(v_{iI}^{\mathrm{s},n} + \dot{v}_{iI}^{\mathrm{s},n+1/2}\Delta t)n_{iI}}{m_I^{\mathrm{f}} + m_I^{\mathrm{s}}} \tag{79}$$

Applying Eqs. (69) and (70) into Eq. (79) leads to

$$v_{iI\mathrm{nor}}^{n+1} = \frac{v_{iI}^{n}(m_I^{\mathrm{f}} + m_I^{\mathrm{s}})n_{iI} + (f_{iI}^{\mathrm{f}} + \tilde{f}_{iI}^{\mathrm{f}} + f_{iI}^{\mathrm{s}} + \tilde{f}_{iI}^{\mathrm{s}})\Delta t n_{iI}}{m_I^{\mathrm{f}} + m_I^{\mathrm{s}}} \tag{80}$$

$$= v_{iI}^{n}n_{iI} + \frac{f_{iI}^{\mathrm{f}} + f_{iI}^{\mathrm{s}}}{m_I^{\mathrm{f}} + m_I^{\mathrm{s}}}\Delta t n_{iI} \tag{81}$$

Noting that by assuming that the external force of fluid and solid comes only from the FSI coupling, $\tilde{f}_{iI}^{\mathrm{f}} + \tilde{f}_{iI}^{\mathrm{s}} = 0$.

Updating with Eq. (81), the nodal velocity $v_{iI\mathrm{nor}}^{n+1}$ still satisfies the no-slip interaction on the normal direction and the tangential nodal velocity is calculated with Eq. (74) which is not influenced by the FSI force acting on the solid normal direction. Then the final solid nodal velocities are obtained with Eq. (77) and serves as the velocity boundary conditions for fluid with Eq. (78), which means the solid grid illustrated in Fig. 8(c) is chosen to represent the motion of MMALE grid.

Compared with the first method, the computational instability is removed and the time-consuming re-location process is avoided. The solid movement at the interface cells is not restricted by the tangential velocity of fluid, which enhance the computational accuracy in simulating interaction between solid and fluid with significantly different velocities (such as the water-entry problems). The slip fluid–structure-interaction method presented here is only adopted in Section 5.4.

5. Numerical results

In this section, five numerical examples, including the shock-cylinder obstacle interaction, flexible panel deformation induced by shock wave, dam-break water flow through a rubber plate, water entry of a wedge and fragmentation of a cylinder shell induced by blast are studied to investigate the performance of the IALEFEM in modeling different kinds of FSI problems.

5.1. Shock-cylinder obstacle interaction

The shock-obstacle interaction is an important field of research and serves as a classical test case in solving the propagation, reflection and superposition of a shock wave under solid influence. Gross [72] studied this problem experimentally and Kan [49] studied this problem numerically as a test case to examine the ability of IALEMPM.

The computational domain is chosen to be $[-7.5, 7.5] \times [-3.5, 3.5] \times [0, 0.01]$ as illustrated in Fig. 9 and divided into two sub-domains with the moving shock. The two sub-domains are filled with the ideal gas and the non-dimensional initial fluid conditions ahead of and behind the moving shock are prescribed as $(\rho_1, \boldsymbol{v}_1, e_1, \gamma_1) = (3.673715, (2.4198, 0, 0), 6.15552, 1.4)$ and $(\rho_2, \boldsymbol{v}_2, e_2, \gamma_2)$

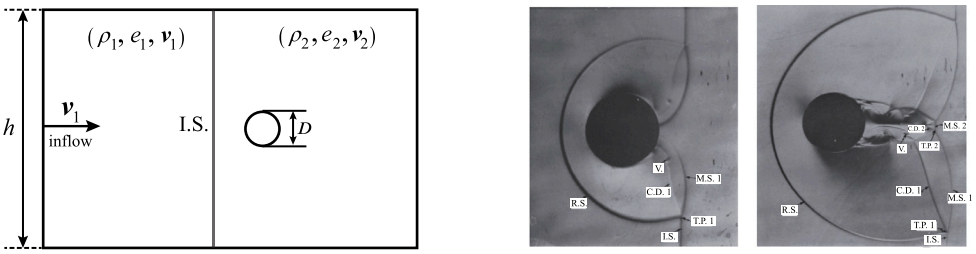

(a) Initial state of shock-cylinder obstacle interaction (b) Experimental results of shock diffraction

Fig. 9. Shock-cylinder obstacle interaction problem and experimental results [72].

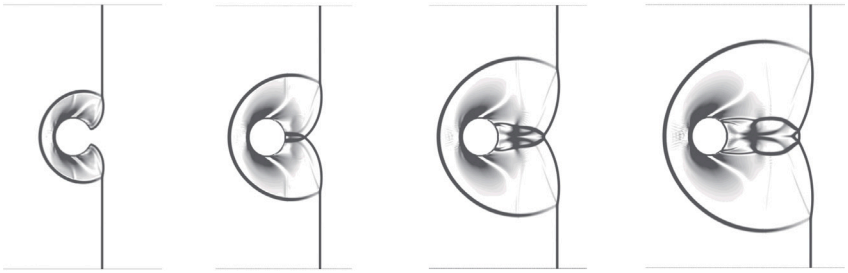

(a) $t = 0.4$ (b) $t = 0.6$ (c) $t = 0.8$ (d) $t = 1.0$

Fig. 10. Numerical shadowgraphs of IALEFEM for shock-cylinder obstacle interaction problem.

= (1, (0, 0, 0), 2.5, 1.4). An inflow boundary condition defined by the inward velocity v_1 is prescribed at the left boundary initially and the outlet condition is adopted at the right boundary. The cell size of the fluid region is $h = 0.01$. The cylinder obstacle is a rigid body discretized into elements with the non-dimensional diameter $D = 1$ and the origin is fixed at $(0.5, 0)$. The initial incident shock is located to the left of the cylinder at $x = -0.5$ with a constant velocity $M_s = 2.81$.

The simulation results of the transient shock wave diffraction and interaction with solid calculated by IALEFEM are shown in Fig. 10. Comparing Fig. 10(a)(c) with the experimental results shown in Fig. 9(b), the early and later shock diffraction are both well captured by the proposed IALEFEM. The incident shock (IS), reflected shock (RS), first and second Mach shock (M.S.1 and M.S.2), contact discontinuity (C.D.1 and C.D.2) and the first and second triple point (T.P.1 and T.P.2) are correctly reproduced. The triple point trajectories for T.P.1 and T.P.2 obtained by the IALEFEM are compared with the experimental results of Gross [72] and numerical results of Chaudhuri [10] and IALEMPM [49] as illustrated in Fig. 11 which shows that IALEFEM gives satisfactory simulation results.

As a summary, the correctness and capacity of IALEFEM is verified by the accurate reproduction of shock diffraction process and complex shock-structure interactions with Mach reflection. The IALEFEM can simulate the shock propagation, reflection and superposition well under the influence of solid.

5.2. Flexible panel deformation induced by shock wave

The flexible panel deformation induced by shock wave has been studied experimentally [73] and numerically [9,73,74]. In this section, this problem will be simulated to examine the ability of IALEFEM in dealing with the complex fluid–structure-interaction.

The computational domain of this problem is shown in Fig. 12 with the height of $H = 80$ mm and is divided into two sub-domains by the incident shock (I.S.). The initial flow states behind the shock are prescribed as $(\rho_1, \boldsymbol{v}_1, p_1, \gamma_1)$ = (1.6548 kg/m^3, (112.61 m/s, 0, 0), 156.18 KPa, 1.4) and the flow states ahead of the shock are $(\rho_2, \boldsymbol{v}_2, p_2, \gamma_2)$ = (1.2 kg/m^3, (0, 0, 0), 100 KPa, 1.4), both of which are of the ideal gas EOS. The inflow boundary conditions are imposed on the left-hand side and the other boundaries are defined as rigid wall.

The flexible panel with the height of $h_2 = 50$ mm and thickness of $d = 1$ mm is clamped into a rigid forward-facing step with the length of $l_1 = 265$ mm and height of $h_1 = 15$ mm. The distance between the flexible panel and the right-hand side of the domain is $l_2 = 250$ mm and the initial position of the shock front is located on the left of the step with the distance of $l_3 = 15$ mm. The flexible panel has a density of $\rho_s = 7.6 \times 10^{-3}$ g/mm^3, Young's modulus of $E_s = 220$ GPa and Poisson's ratio of $\nu = 0$.

The fluid domain is discretized with the cell size of 0.25 mm and solid domain is discretized with element size of 0.125 mm. The computational results obtained with the IALEFEM are compared with the experimental shadowgraphs and numerical results of Giordano [73] as depicted in Fig. 13. The time $t = 0$ μs is defined as the instant when the incident shock wave interacts with the panel [73] and the time interval is 70 μs.

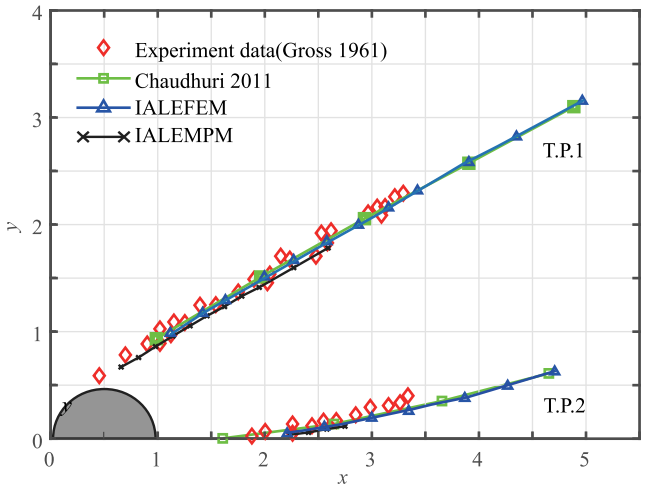

Fig. 11. Trajectories of the Mach shock triple points T.P.1 and T.P.2.

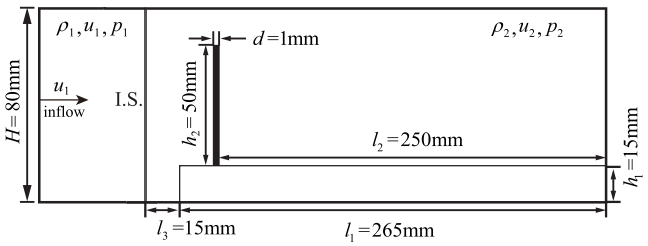

Fig. 12. Computational domain for simulation of flexible panel deformation induced by shock wave.

The numerical results obtained by IALEFEM are in good agreement with experimental and numerical results of Giordano et al. [73]. After interacting with the solid, the reflected waves are generated and apply the bending load on the panel. Then the vortex are produced by the roll-up of the slipstream on the panel top tip and then moves out from the panel. Meanwhile the Mach reflection upon the top surface of the forward-facing step can also be observed and the location of the fluid structures is in good agreement with the results of Giordano.

The x-displacement of the flexible panel top tip versus time is illustrated in Fig. 14 in which IALEFEM is in good agreement with the experimental data and numerical results of Giordano et al. [73] and Ni et al. [11] in the time of peak value and the largest displacement. The largest x-displacement obtained by IALEFEM is 6.64 mm (the relative error = 7.6%) and the time of peak value is 1.34 ms (the relative error = 0.4%), which also fits well with the numerical results of partitioned FSI methods [11,73,74]. With the immersed boundary method (IBM), Giordano et al. [73] coupled the finite volume method for fluid solver and the FEM for structure solver while Tian et al. [74] adopted the finite difference method for the fluid and the FEM beam for the structure. Ni et al. [11] also presented a Lagrangian continuous-forcing IBM to couple the FVM for fluid and MPM for structure (IBMPM). With the adoption of FEM, IALEFEM can remove the cell crossing noise of MPM and improve the computational accuracy in simulating finite deformation of structures compared with IBMPM. Meanwhile the monolithic FSI coupling is realized through the MMALE grid, which makes the IALEFEM also available for simulating incompressible fluid–structure interaction and complex multi-phase flow problems more stably while being unaffected by the artificial added mass instabilities [24] within partitioned FSI methods with sequentially staggered schemes.

5.3. Dam-break water flow through a rubber plate

The deformation of an elastic plate under the dam-break water flow presented by Antoci et al. [75] is usually adopted to test the correctness of the fluid–structure-interaction method in dealing with incompressible flow. In this section, this problem is also simulated with IALEFEM. The diagram of the problem is illustrated in Fig. 15 in which the water domain $[0, 100\ \text{mm}] \times [0, 140\ \text{mm}] \times [0, 1\ \text{mm}]$ and the rest with the air. The rubber gate is fixed at its upper end and free at the bottom end. The height and thickness of the plate is 79 mm and 5 mm respectively.

With the IALEFEM, the fluid domain is discretized into MMALE cells with the cell size of 1 mm and the solid domain is discretized into FEM elements with the element size of 0.5 mm. The water has a density of 1000 kg/m^3 and dynamic viscosity of 1×10^{-3} Pa·s, which is simulated with the weak compressible EOS. The artificial sound speed is chosen as 50 m/s [71] to increase time step size,

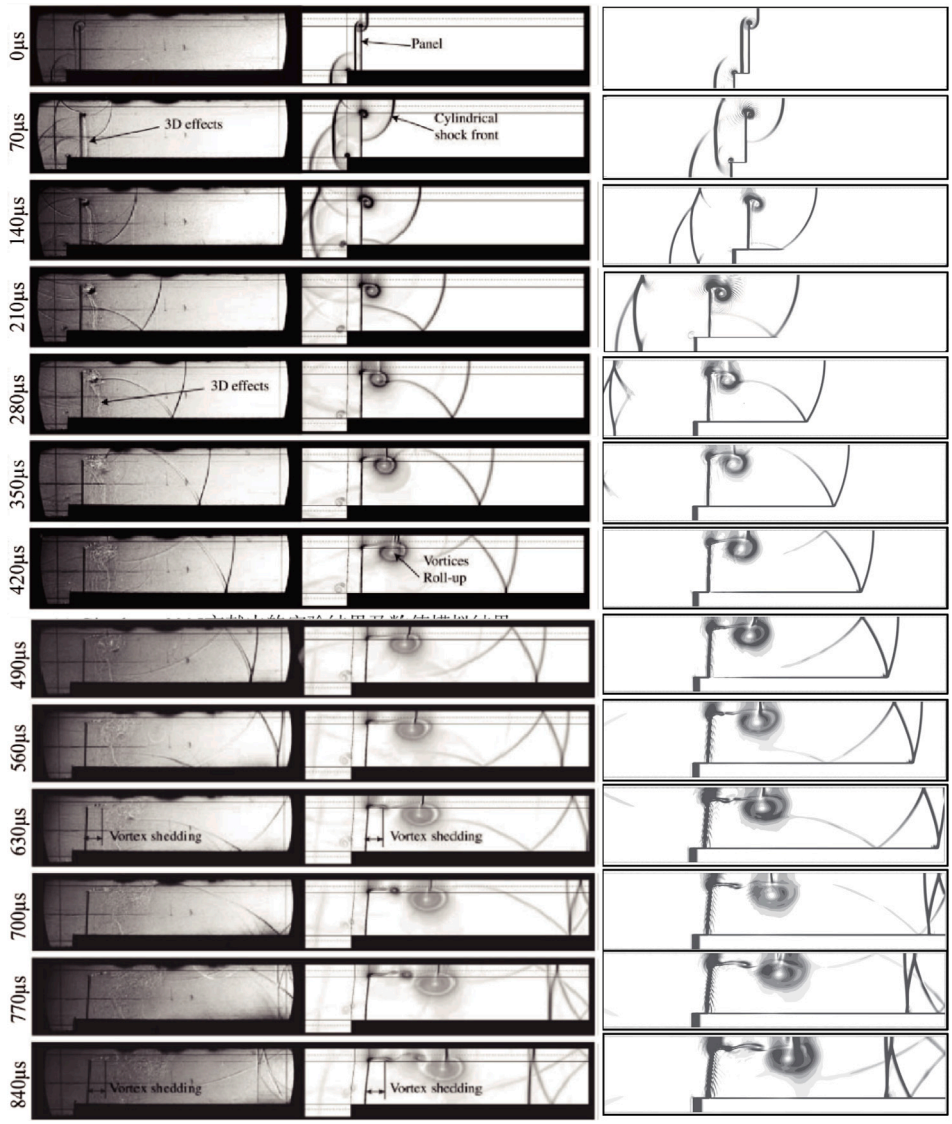

(a) Experimental results of Giordano (b) Numerical results of Giordano (c) Numerical results of IALEFEM

Fig. 13. Numerical results of the shock-panel interaction simulation from 0 μs to 840 μs per 70 μs.

limit density fluctuations and avoid pressure oscillation [76]. The air is of the ideal gas EOS with the density of 1.29×10^{-6} g/mm^3, $\gamma = 1.4$ and internal energy per unit volume of 0.25 mJ/mm^3. The rubber plate is simulated with the linear elastic constitutive model and has a density of 1100 kg/m^3, the Young's modulus of 10 MPa and Poisson's ratio of 0.4 according to the literature [75]. Symmetric boundary conditions are applied for the z-axis boundaries to simulate the 2D case while the other boundaries are defined as rigid wall.

The numerical results of IALEFEM and experimental results [75] from 0.04 s to 0.16 s are depicted in Fig. 16. Comparing with the experimental results, IALEFEM simulates the fluid–structure-interaction accurately and gives satisfactory numerical results. The water drops and flows through the rubber plate to the right side of the fluid domain. Meanwhile the plate experiences large deformation under the water pressure. The rubber plate rebounds when the water level drops and the pressure decreases. As illustrated in Fig. 16(c)(d), some water leakage occurs beside the rubber plate [75], resulting in the water level obtained by IALEFEM being slightly higher than the actual one.

The horizontal and vertical displacements at the bottom end of the rubber gate versus time obtained by IALEFEM are illustrated in Fig. 17 to represent the structural deformation and compared with the experimental data [75] and the numerical results by Antoci et al. [75], Rafiee et al. [77], Yang et al. [78], Khayyer et al. [79] and Li et al. [46]. Compared with other numerical methods, the results of IALEFEM agree well with the experimental results in the time of peak value and the largest horizontal displacement, which

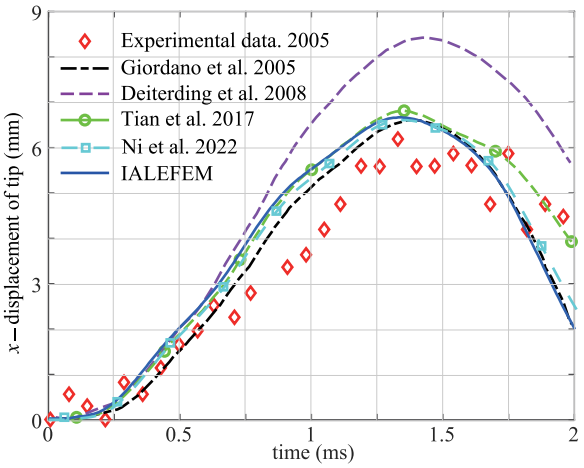

Fig. 14. x-Displacement of the flexible panel top tip for 2 ms.

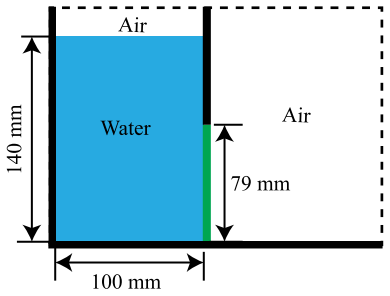

Fig. 15. Problem description of dam-break water flow through a rubber plate.

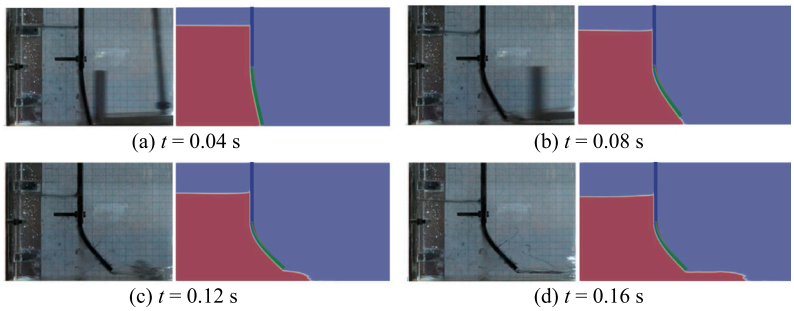

Fig. 16. Numerical results of dam-break water flow through a rubber plate at different time (t = 0.04 s, 0.08 s, 0.12 s, 0.16 s) compared with experimental results [75].

shows the accuracy of the proposed method in simulating complicated FSI problems with large deformations. The largest horizontal displacement obtained by IALEFEM is 0.0435 m with the relative error 4.6%. Regarding the vertical displacement, the peak value obtained by IALEFEM appears earlier than the experimental data but the largest vertical displacement 0.01696 m (the relative error = 0.24%) obtained by IALEFEM is still consistent with the experimental data (0.017 m). In the later stage of simulation, there are some differences between the experimental data and numerical result of IALEFEM which is close to the numerical result of Rafiee et al. [77].

5.4. Water entry of a wedge

The water entry of a wedge with splash under gravity is simulated in this section. The experiment of this problem is conducted by Zhao et al. [80]. As illustrated in Fig. 18, the wedge is 0.5 mm wide and has a mass of 241 kg. The acceleration of gravity is

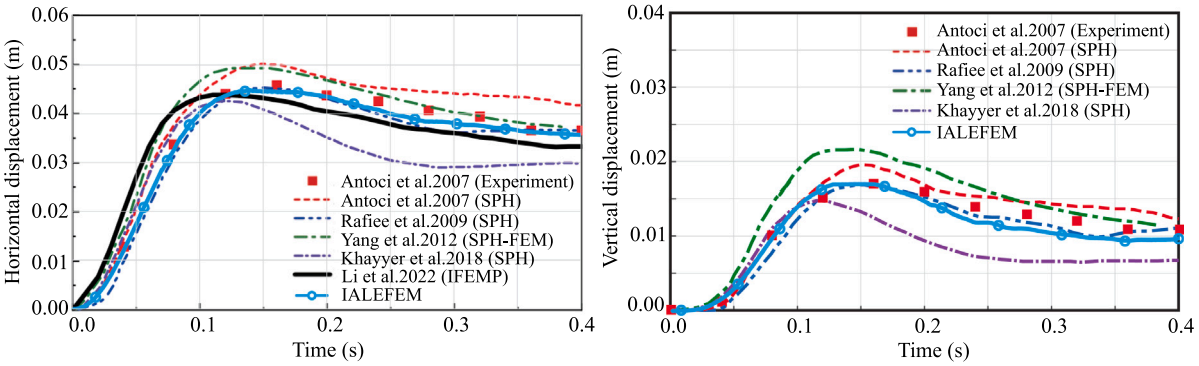

Fig. 17. Horizontal and vertical displacements at the bottom end of the rubber gate obtained by IALEFEM and compared with experimental data by Antoci et al. [75] and numerical results by Antoci et al. [75], Rafiee et al. [77], Yang et al. [78], Khayyer et al. [79] and Li et al. [46].

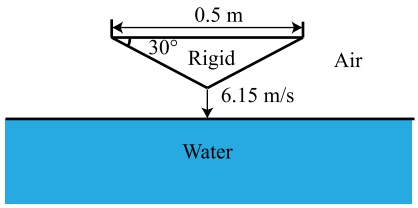

Fig. 18. Simulation set-up of water entry.

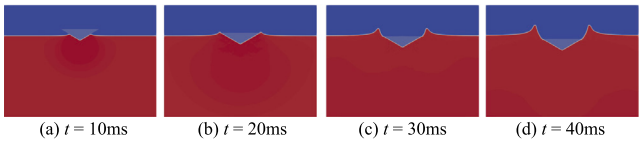

Fig. 19. Evolution of fluid domain with wedge motion at different time (t = 10 ms, 20 ms, 30 ms, 40 ms).

taken to be $g = 9.81$ m/s^2 and the initial velocity of the wedge is 6.15 m/s when interacted with the water. The water is located in a tank with a depth of 1 m and width of 2 m.

The problem is simulated with the plain strain assumption. The fluid domain [0, 2 m] × [0, 1.5 m] × [0, 0.005 m] is discretized with MMALE cells with cell size of 0.005 m and the solid wedge is discretized by 26000 hexahedral elements. The wedge is set as rigid body with very large Young's modulus $E = 10^7$ MPa, while the water is modeled by the null material with incompressible EOS. The artificial sound speed is chosen as 50 m/s to avoid the pressure oscillation [81]. The air is simulated with the ideal gas EOS with $\gamma = 1.4$, $\rho_{\text{air}} = 1.29 \times 10^{-6}$ g/mm^3 and internal energy per unit volume $E_{\text{air}} = 0.25$ mJ/mm^3. Symmetric boundary conditions are applied for the z-axis boundaries to simulate the 2D case.

The evolution of the interaction between the wedge and fluid obtained by slip IALEFEM is illustrated in Fig. 19 with the time interval 10 ms. The water splash caused by the wedge falling can be observed with a smooth shape. Furthermore, the time history of the wedge velocity obtained by IALEFEM is presented in Fig. 20 and is compared with the experimental result by Zhao et al. [80] and the numerical results using weakly compressible MPM by Chen et al. [71] and level set immersed boundary method by Zhang [82]. Both the slip and no-slip FSI methods of IALEFEM give good prediction with experiment data before $t = 0.016$ s, but the velocity is underestimated in the later period. With the adoption of slip FSI method, the wedge velocity obtained by IALEFEM achieve better results compared with the no-slip interaction method and is closer to the experimental data as well as other numerical methods.

5.5. Fragmentation of a cylinder shell induced by blast

This section simulates the fragmentation of a 1045 steel cylindrical shell under blast loading [83], which is a challenging and complicated problem with dynamic fracture and multi-material fluid flow. The MPM [84] and IALEMPM [49] have been applied to this problem with the steel shell discretized by particles.

This problem is simplified into a plain strain problem and a 1/4 model is adopted due to symmetry as shown in Fig. 21. The explosive used in the experiment is RHT-901 and is placed inside the cylindrical shell with outer radius of 30 mm and inner radius of $r = 20$ mm. The inner radius and thickness of the cylindrical shell are $R = 30$ mm and $d = 4$ mm. The air is surrounding the explosive and shell.

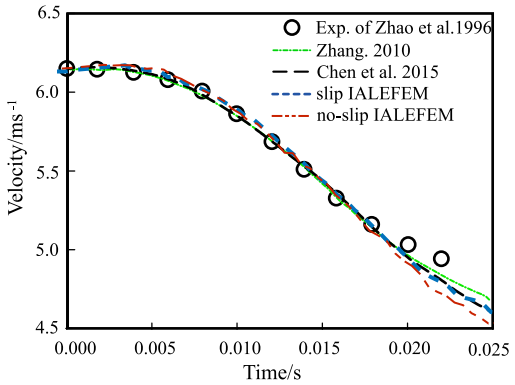

Fig. 20. Wedge velocity obtained by IALEFEM compared with the experimental data [80] and other numerical results [71,82].

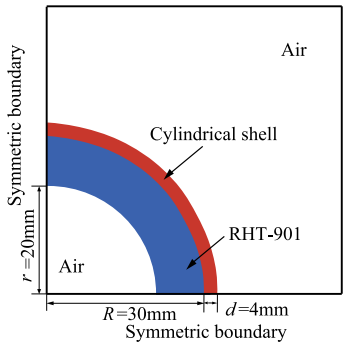

Fig. 21. Simulation set-up of cylindrical shell fragmentation driven by detonation.

Table 1
The constants of Gurson model for 1045 steel [88].

q_1	q_2	f_{0e}	f_{0s}	f_f	f_c	f_N	ϵ_N	s_N	ϵ_f
1.5	1	0.005	0.0003	0.0021	0.2109	0.001	0.04	0.01	0.43

With the IALEFEM adopted, the fluid domain is chosen as $[0, 75\ \text{mm}] \times [0, 75\ \text{mm}] \times [0, 0.5\ \text{mm}]$ with the cell size of 0.5 mm. The explosive has a density of $\rho = 1.684 \times 10^{-3}$ g/mm^3 and internal energy per unit volume of $E_0 = 6853.9$ mJ/mm^3 and adopt the JWL equation of state with the parameters $A = 524.2$ GPa, $B = 0.0321$ GPa, $R_1 = 4.15$, $R_2 = 0.95$, $\omega = 0.3$ [85]. The ideal gas EOS is adopted for the surrounding air with the density of $\rho_{\text{air}} = 1.2 \times 10^{-6}$ g/mm^3, the internal energy per unit volume $E_0 = 0.266772$ mJ/mm^3 and $\gamma = 1.4$.

The steel shell is described by the simplified Johnson–Cook model as

$$\sigma_y = \left(A + B\bar{\epsilon}_p^n\right)\left(1 + C \ln \dot{\epsilon}_p^*\right) \tag{82}$$

where $A = 5.07{\times}10^5$MPa, $B = 3.2{\times}10^3$MPa, $n = 0.28$, $C = 0.064$ [86] and Gurson model [87] with TEPLA-F failure condition to model the microscopic defects, which is discretized into 11 781 hexahedral elements. The fracture strain ϵ_f of the cylinder shell is measured to be 0.43 in Tang [83] and the other parameters of Gurson model for 1045 steel are shown in Table 1. The Mie–Gruneisen EOS is adopted to update the volumetric stress of steel shell with parameters $c_0 = 3570$ mm/ms, $s_1 = 1.92$ and $\gamma_0 = 1.8$. The boundary conditions at $x = 0$ mm and $y = 0$ mm are symmetric boundaries while boundary conditions at $x = 75$ mm and $y = 75$ mm are outlet boundaries.

The density contours of the fluid obtained by IALEFEM from 0 μs to 40 μs are shown in Fig. 22 compared with the results of IALEMPM. At the beginning of simulation, an blast wave is generated and drive the cylindrical shell to expand. The products of the explosive expands to nearly the whole interior of the shell and the air inside the cylindrical shell is compressed into the origin with very little volume. After a period of time, a shock wave reflects from the symmetry boundary and drives the shell fragments to accelerate. In the early stage of simulation, the density results of explosive gas in IALEMPM are as good as those of IALEFEM. Stationary flow, implosion wave and reflection wave can all be captured clearly. However, with time increasing and structural fragmentation, the explosive gas flows out from the fragments and IALEFEM gives more reasonable and symmetrical density contours the circumferential direction.

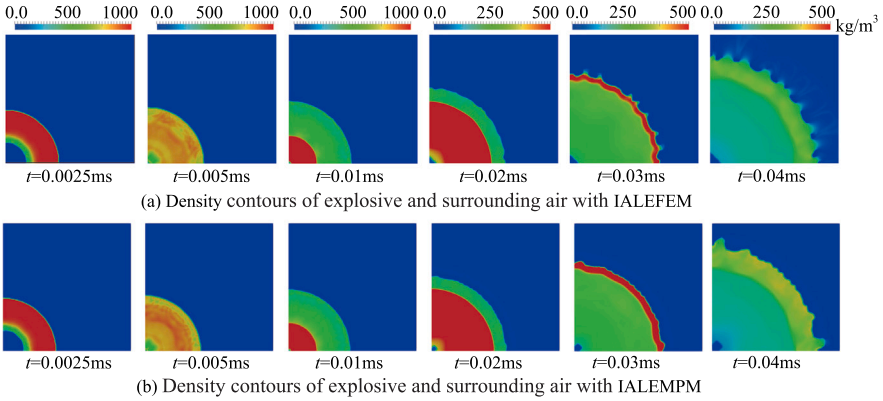

Fig. 22. Density contours of explosive and surrounding air from 0 μs to 40 μs.

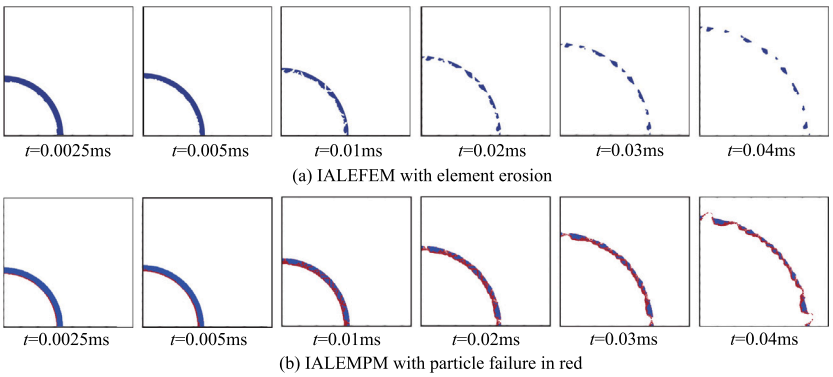

Fig. 23. Numerical results of cylinder shell fragments contour from 0 μs to 40 μs.

Table 2
Statistics of fragments' midline width and thickness at the end of simulation (Unit: mm).

Simulation method	Midline-width/Thickness of main fragments						Average width/thickness
IALEMPM	3.30/2.84	6.99/4.06	7.86/2.36	7.32/4.50	5.59/2.93	4.50/2.44	5.87/3.14
	5.74/2.80	6.06/3.57	11.3/4.75	3.59/2.41	2.35/1.85		
IALEFEM	4.74/3.52	8.66/2.42	6.51/3.29	5.82/2.92	8.86/2.63	5.16/3.19	6.63/3.00
Experiment [83]	/						7.86/3.3

The fragments contours of the cylindrical shell are shown in Fig. 23 to compare the whole process of fracture. The IALEFEM adopts the element erosion to denote the material failure and fragments are then generated clearly, while the IALEMPM simulates the structural failure with particle failure and numerical fracture. Failure particles are unable to sustain the tensile force. At the beginning of the dynamic fracture process, the inner side of the shell fail with shear instability under the impact of high pressure explosive which can be captured by both methods. Then with severe plastic deformation and expansion of the shell, the cracks caused by shear localization propagate from the inner side of the shell to the outer side and finally forms the fragments in IALEFEM while IALEMPM gives more severe tensile fracture at the outer side of the shell in the early stage as illustrated in Fig. 23. The appearance time of first crack calculated by the IALEFEM is 9.2 μs and is closer to the 8.8 μs of the experiment [83] compared with 8.0 μs by the IALEMPM, which means IALEMPM simulates more severe failure of the shell.

The midline width and thickness of main fragments are shown in Table 2 and compared with the experiment results [83]. The IALEFEM obtains better results in midline width and worse results in thickness due to the adoption of element erosion. With the motion of the solid, elements are deleted with structural failure which causes non-conservation of mass and computation error. The computational error of IALEMPM is caused by the cell crossing noise of MPM and spurious strain calculated with mixed velocity field, which leads to more severe fragmentation in the circumferential direction.

The CPU time calculated by IALEMPM and IALEFEM (with and without OpenMP parallel implementation) is compared to illustrate the computational efficiency of the presented method, as shown in Table 3. The physical time, computational domain, and other computational conditions are consistent across different methods. The CPU time obtained by IALEMPM and IALEFEM without

Table 3
CPU time of IALEMPM and IALEFEM with and without OpenMP parallel implementation.

Simulation method	IALEMPM	IALEFEM(1 thread)	IALEFEM (2 threads)	IALEFEM (3 threads)
CPU time/s	899.4	888.8	475.9	351.4

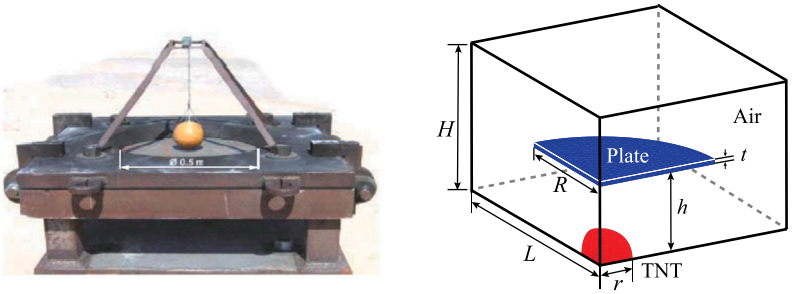

(a)Experimental setup (b) Computational model

Fig. 24. The experimental devices [89] and computational model of IALEFEM. (For interpretation of the references to color in this figure legend, the reader is referred to the web version of this article.)

OpenMP parallel implementation is calculated simultaneously on the same computer equipped with an Intel(R) Core™ i9-11900K CPU (3.50 GHz) and a 64-bit Windows operating system. The IALEFEM requires less CPU time than IALEMPM and demonstrates better computational efficiency, as shown in Table 3. With OpenMP parallel implementation applied in the Euler phase, the CPU time decreases significantly with the number of threads, indicating that the CPU time is primarily consumed by the Euler phase.

5.6. Response of elastic plate subjected to spherical near-field explosion

In this section, a metal circular plate subjected to near-field blast loading is investigated using IALEFEM. This 3D problem has been studied experimentally by Neuberger [89] as depicted in Fig. 24(a) and the maximal vertical displacement of the plate was obtained. The plate undergoes large deformation under blast loading and the structural response is predominantly dynamic elastic [89].

Due to symmetry, a 1/4 computational model is adopted for this problem, as shown in Fig. 24(b). The TNT explosive shown in red is placed at the origin (0 m, 0 m, 0 m) with the radius of $r = 0.041$ m and its total mass is 0.468 kg. The circular plate shown in blue is located at a distance of $h = 0.1$ m from the origin and has a radius of $R = 0.25$ m and thickness of $t = 0.01$ m. The air surrounds the explosive and circular plate. Using the IALEFEM, the fluid domain [0, 0.3 m] × [0, 0.3 m] × [0, 0.17 m] is discretized into 122,400 MMALE cells.

The TNT explosive has a density of $\rho = 1.63 \times 10^{-3}$ g/mm^3 and an internal energy per unit volume of $E_0 = 7000$ mJ/mm^3. The JWL equation of state is used to model the explosive products [90] with the parameters $A = 371.2$ GPa, $B = 3.23$ GPa, $R_1 = 4.15$, $R_2 = 0.95$, and $\omega = 0.3$. The ideal gas EOS is adopted for the surrounding air, which has a density of $\rho_{\text{air}} = 1.225 \times 10^{-6}$ g/mm^3, an internal energy per unit volume $E_0 = 0.266772$ mJ/mm^3, and $\gamma = 1.4$.

The circular plate, made of RHA steel, is discretized into 48 190 hexahedral elements. The Young's modulus of the RHA steel is 210 GPa and Poisson's ratio is 0.28. The RHA steel is modeled by the simplified Johnson–Cook constitutive equation [89]

$$\sigma_y = (A + B\varepsilon^{pn})(1 + C \ln \dot{\varepsilon}) \tag{83}$$

where σ_y is the yield stress, $A = 950$ MPa, $B = 560$ MPa, $n = 0.26$ and $C = 0.014$. The Mie–Gruneisen equation of state [91]

$$P = P_H \left(1 - \frac{\gamma\mu}{2}\right) + \gamma\rho e \tag{84}$$

is adopted to simulate the state variables of RHA steel, where $\mu = \rho/\rho_0 - 1$ and $\gamma = 1.67$,

$$P_H = \begin{cases} \rho_0 C_0^2 \left[\mu + (2S-1)\mu^2 + (S-1)(3S-1)\mu^3\right] & \mu > 0 \\ \rho_0 C_0^2 \mu & \mu < 0 \end{cases} \tag{85}$$

with $\rho_0 = 7.85 \times 10^{-3}$ g/mm^3, $C_0 = 4610$ m/s and $S = 1.49$.

The symmetric boundaries are set at the surfaces where $x = 0$ m, $y = 0$ m and $z = 0$ m, while the other three surfaces are set as pressure boundaries with the same pressure as the surrounding air. The physical time is set as $t = 0.6$ ms to obtain the maximal vertical displacement of the plate.

Typical contours of fluid pressure and plate deformation at different time are illustrated in Fig. 25 and compared with the contours obtained by IALEMPM [49]. The generated shock wave expands towards the circular plate and drives the plate to bend after interaction. As the plate is clamped at the boundary, the midpoint of the plate experiences large deformation. Meanwhile the

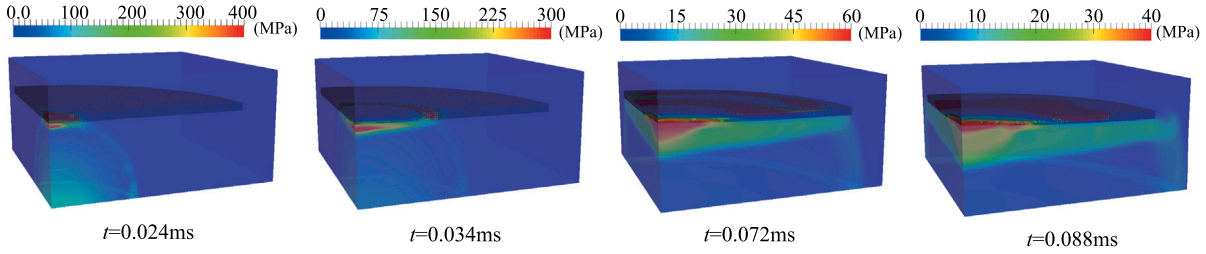

(a) Fluid pressure contours and deformed plate obatined by IALEMPM

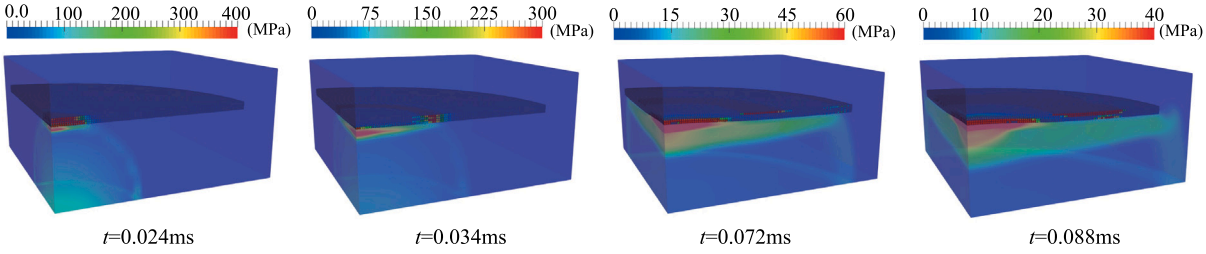

(b)Fluid pressure contours and deformed plate obatined by IALEFEM

Fig. 25. Fluid pressure contours and deformed plate at different time (t = 0.024 ms, 0.034 ms, 0.072 ms, 0.088 ms) obtained by IALEFEM and IALEMPM [49].

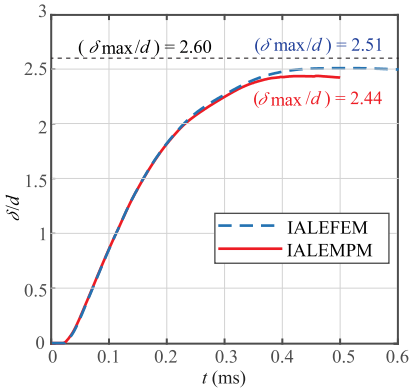

Fig. 26. Displacement histories of the plate center obtained by IALEFEM and IALEMPM [49].

explosive and shock wave reflect and propagate along the radial direction of the plate. Both IALEFEM and IALEMPM reproduce the whole process, and the pressure contours are similar in the early stage. However, since the fluid–structure interaction is imposed differently through respective methods of solid force calculation, the propagation process of fluid and solid deformation simulated by IALEFEM is slightly delayed compared with IALEMPM.

According to the experiment [89], the maximal displacement of the plate occurs at its center and the ratio of the maximal displacement to the plate thickness is $\delta_{\max}/d = 2.60$. The displacement histories of the plate center obtained by IALEFEM and IALEMPM are illustrated in Fig. 26, in which IALEFEM achieves a better simulated ratio of $\delta_{\max}/d = 2.50$ compared with $\delta_{\max}/d = 2.44$ in IALEMPM. The displacement obtained by IALEFEM continues to increase until around 0.5 ms, while the plate simulated by IALEMPM starts to rebound at 0.46 ms.

Fig. 27 illustrates the von Mises stress contours of the plate over a time span of 0.5 ms. The magnitude of the von Mises stress increases gradually and IALEFEM gets smoother equivalent stress contours, which is due to the avoidance of cell crossing noise when the FEM is employed for the solid. The mixed velocity field, which can cause spurious stress [50], is also eliminated as the solid stress is updated using FEM nodal velocities rather than the mixed MMALE nodal velocities. The CPU time for this problem is measured on a computer equipped with an Intel(R) Xeon(R) Gold 6248R CPU (3.00 GHz) and a 64-bit Linux operating system. With OpenMP parallel implementation of 30 threads for the Euler phase, IALEFEM takes 3.43 h for the calculation, which is less than 3.63 h consumed by IALEMPM with the same 30 threads for the Euler phase.

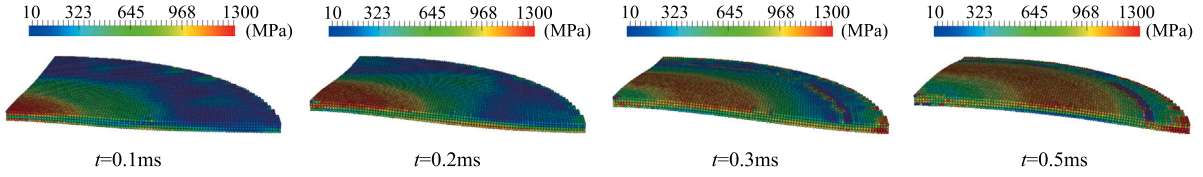

(a) Von Mises stress contours of the plate obatined by IALEMPM

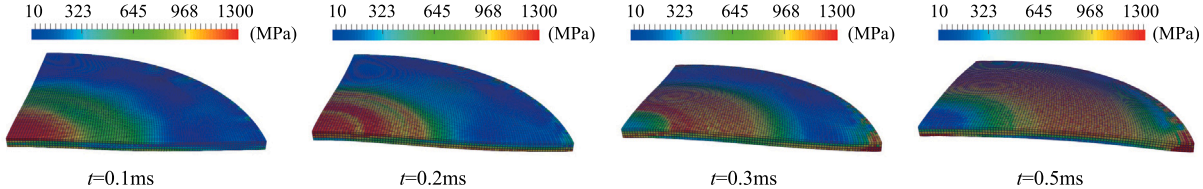

(b) Von Mises stress contours of the plate obatined by IALEFEM

Fig. 27. Von Mises stress contours of the plate at different time (t = 0.1 ms, 0.2 ms, 0.3 ms, 0.5 ms) obtained by IALEFEM and IALEMPM [49].

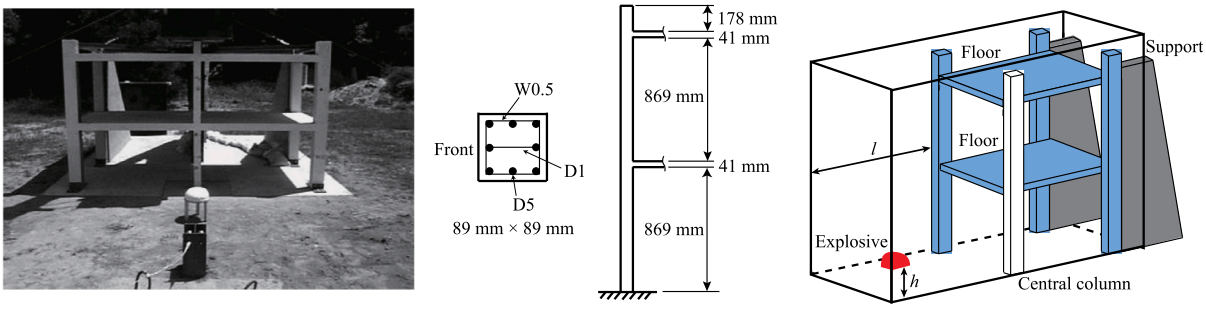

(a)Experimental set-up (b) Exterior central column details (c) Computational model

Fig. 28. Experimental set-up [92,93], exterior central column details [93] and computational model of open-frame building under explosion.

5.7. Structural damage of open-frame building under blast loading

Woodson and Baylot [92] tested a 1/4-scale reinforced concrete frame building to study the structural damage and dynamic response of the central column under blast loading. Baylot and Bevins [93] numerically studied this problem using CTH code for blast loads and LS-DYNA for structural damage. The reinforced concrete column in this structure has also been numerically studied by Shi et al. [94], Chen et al. [95], and Li et al. [96].

The building tested in the experiment [92,93] is a two-story reinforced concrete frame, which is 3.20 m wide and 1.53 m deep, and is composed of two floors and six columns, as illustrated in Fig. 28(a). The primary focus of the study is the exterior central column located directly in front of the explosive, which has a cross section of 89 mm by 89 mm, as shown in Fig. 28(b). The hemispherical C4 explosive is positioned 1.07 m horizontally from the building and at 0.305 m above the ground. The explosive has a mass of 7.1 kg and can be equivalent to 8.449 kg TNT based on the same impulse [93]. Due to symmetry, a 1/2 computational model is simulated here by IALEFEM, as shown in Fig. 28(c).

The computational domain has a size of L = 3.15 m, D = 2.025 m and H = 2.25 m which is discretized into 1260000 MMALE cells. A 1/8 spherical TNT explosive with the mass of 2.11225 kg is used here due to symmetry. The TNT has a density of 1.63×10^{-3} g/mm^3 and is modeled using the JWL equation of state with the same parameters as in Section 5.6: A = 371.2 GPa, B = 3.23 GPa, R_1 = 4.15, R_2= 0.95, and w = 0.3. The ideal gas EOS is also applied to the air with the same parameters as in Section 5.6. The non-reflecting boundaries are implemented at the surfaces of x = 3.15 m, y = 2.025 m, and z = 2.25 m for the outer periphery of the air, while symmetric boundaries are applied for the other boundaries.

The concrete used in the structure has a density of 2.068×10^{-3} g/mm^3, a Young's modulus of 28.7 MPa, and a Poisson's ratio of 0.19. The HJC model is employed to simulate the mechanical behavior and damage of the concrete, and the material parameters are shown in Table 4 which are taken from the literature [93].

Three kinds of principal rebars are used in the central column, which consist of eight deformed wire bars (D5), column ties (W0.5) and shear reinforcement (D1), as shown in Fig. 28(b). The rebars are described by the linear strengthening plastic model with density $\rho = 7.5 \times 10^{-3}$ g/mm^3, Young's modulus E= 200 GPa and Poisson's ratio $\upsilon = 0.3$. The yield strength, ultimate strength and geometry sizes are listed in Table 5, which is taken from the literature [93]. The structure is fixed to the ground and the total number of finite elements is 404,121.

Table 4
The parameters of HJC material model.

A	B	n	C	f_c'/MPa	S_{max}	T/MPa	D_1	D_2	$\epsilon_{f\ min}$
0.79	1.60	0.61	0.007	42	7.0	4.1	0.04	1.0	0.001
p_{crush}/MPa	μ_{crush}	p_{lock}/GPa	μ_{lock}	K_1/GPa	K_2/GPa	K_3/GPa			
12	0.001	0.8	0.10	85	−171	208			

Table 5
Geometry size and properties of reinforcement [93].

Reinforcement	Area(mm^2)	Yield stress(MPa)	Ultimate strength
W0.5	3.22	441	513
D1	6.45	399	610
D5	32.2	449	513

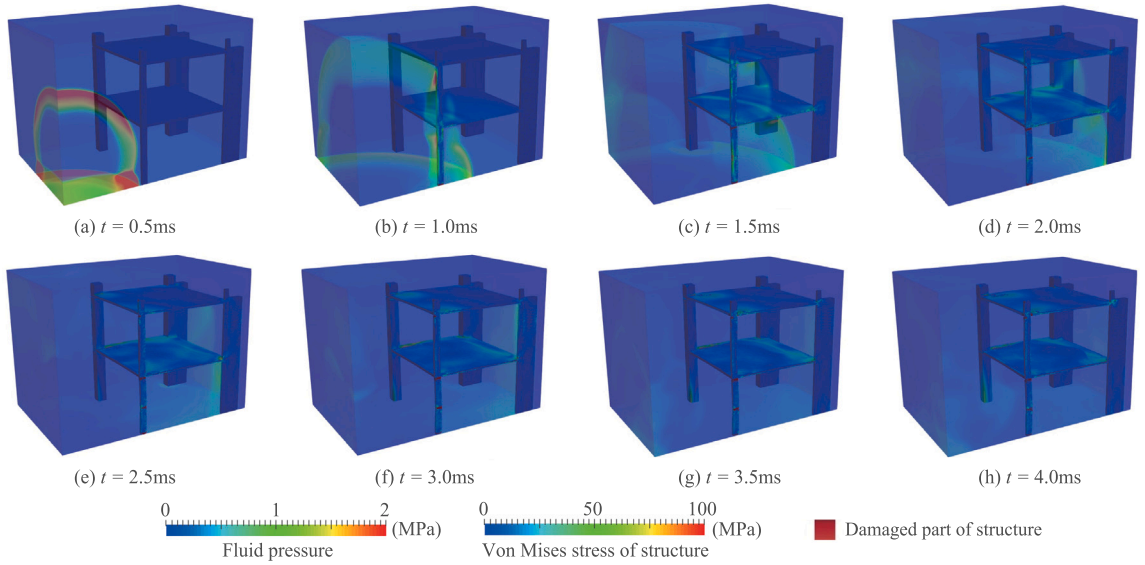

Fig. 29. Damage, pressure and von Mises stress contours at different time of open-frame building and fluid domain. (For interpretation of the references to color in this figure legend, the reader is referred to the web version of this article.)

With IALEFEM employed, the interaction process of the shock wave induced by blast and the building is simulated, and the typical contours of fluid pressure and structural von Mises stress are illustrated in Fig. 29. Damaged parts of the structure are also depicted in red. Following the explosion, the shock wave is generated and reflects at the ground, forming a Mach reflection wave as illustrated in Fig. 29(a). Subsequently, the shock wave propagates and interacts with the central column at $t = 0.62$ ms. Under the overpressure of the explosion wave, the column bends and structural damage occurs near the lower support where high plastic strain is also present (Fig. 29(b)). The upper support also experiences damage due to the flexural and shear stress, as depicted in Fig. 29(c). Due to the reflection of stress waves, the back of the central column is subjected to tensile waves, and damage cracks appear and grow along the mid-height of the central column, which can be observed in Fig. 29(d)–(h). Meanwhile the shock reflection, propagation, superposition, and diffracted waves around the structure can also be observed in Fig. 29 as well as the structural deformation, which demonstrates the capacity and correctness of IALEFEM.

Under blast loading, the central column undergoes large deformation and rebounds with multiple vibrations. In this section, the physical time is set to 8 ms to record the peak displacement of the central column, which occurs in the first vibration process. The displacement history at the mid-height of the column obtained by IALEFEM is illustrated in Fig. 30 and compared with other numerical simulations and experimental data. It should be noted that the origin of the time axis in Fig. 30 is adjusted to the time when the central column begins to deform. As shown in Fig. 30, the central column in IALEFEM simulation experiences larger deformation compared with the experimental result in the early stage of simulation, which is likely because the actual structure is reinforced at the top of the columns and at the connections between the columns and the floor slabs. The peak displacement obtained by IALEFEM is 11.4 mm (the relative error = 8.80%) at around 3 ms (the relative error = 4.31%) which agrees well with the experimental result by Woodson et al. [92] and the numerical result obtained by Chen et al. [95]. In Chen's study, the central column is simulated using the LS-DYNA finite element (FE) model, and the blast loading is idealized into triangular pressure time history and applied to the column. The computational errors in the time of peak value and largest displacement obtained

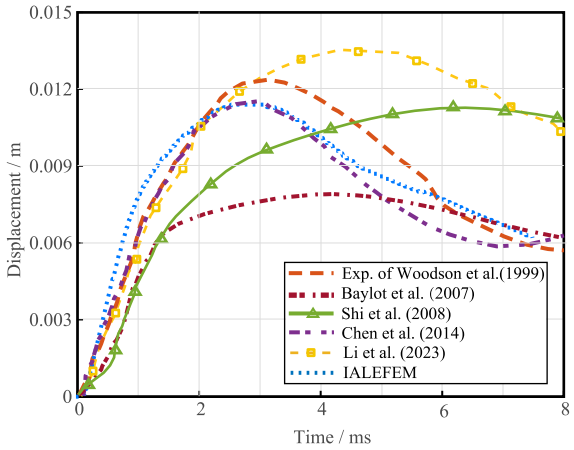

Fig. 30. Displacement history at the mid-height of the central column obtained by IALEFEM and compared with experimental data by Woodson et al. [92] and numerical results by Baylot et al. [93], Shi et al. [94], Chen et al. [95] and Li et al. [96].

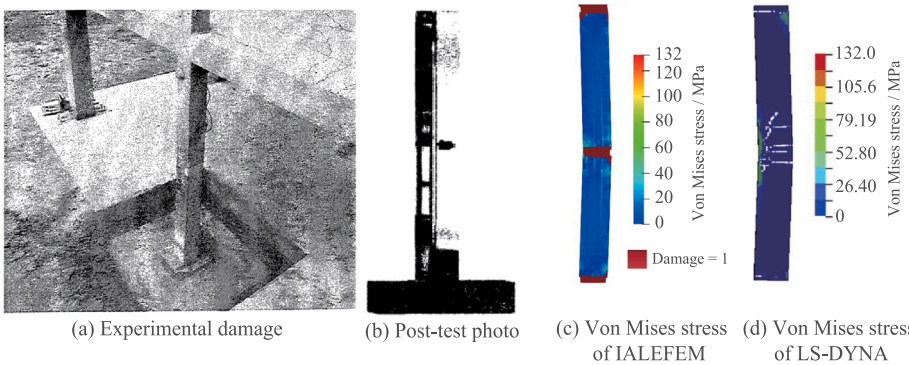

Fig. 31. Comparison of structural damage and von Mises stress contours obtained by IALEFEM with experimental [92] and LS-DYNA [95] results.

by IALEFEM may arise from the differences in explosive properties between C4 and TNT, as 7.1 kg of C4 produces a larger peak pressure than 8.449 kg of TNT according to the literature [93].

Fig. 31 depicts the structural damage in the experiment as well as the von Mises stress contours at $t = 3$ ms obtained by IALEFEM and LS-DYNA [95]. As illustrated in Fig. 31(a)(b), severe damage cracks are formed along the center of the column and near the supports in the experiment, which is captured clearly by IALEFEM in Fig. 31(c). Compared with the numerical results of LS-DYNA [95], the distribution of damage cracks in the mid-height of the column simulated by IALEFEM is more concentrated as shown in Fig. 31(c)(d), which agrees well with the experimental results. Meanwhile, IALEFEM also captures significant damage at the bottom of the central column, as reported in the experiment [92]. The high von Mises stress areas are primarily distributed near the damaged parts of the column, which can be observed in both Fig. 31(c) and (d) with similar values. The experiment also records the peak pressure (7.5 MPa) on the front of the column near the height of the explosive. Compared with the numerical result of 8.1 MPa obtained by LS-DYNA with the Load_Blast_Enhanced (LBE) function [96], IALEFEM simulates more accurate fluid–structure interaction and obtains a peak pressure of 7.78 MPa with a smaller relative error of 3.73%.

Due to the large number of MMALE cells and finite elements, the simulation takes 39.95 h when using 30 threads for the Euler phase on a computer equipped with an Intel(R) Xeon(R) Gold 6248R CPU (3.00 GHz) and a 64-bit Linux operating system. As the Euler phase consumes the majority of the CPU time and is easily parallelized in IALEFEM, parallel computing can significantly enhance the computational efficiency.

6. Conclusions

A novel immersed multi-material arbitrary Lagrangian Eulerian finite element method (IALEFEM) is proposed in the present work for effectively simulating of the fluid–structure interaction problems with multi-phase flow dynamics. The finite element method and the MMALE method are strongly coupled without requiring conforming meshes by immersing the elements into the MMALE grid. The monolithic fluid–structure interaction is realized through the MMALE grid by assembling the nodal forces and momentum of the grid from both the solid and fluid. By adopting the immersed boundary method, the IALEFEM combines the advantages

of FEM in simulating solid materials and the MMALE method in simulating multi-phase fluid flow accurately and efficiently. Additionally, the fluid–solid interface can be accurately and implicitly captured by the boundaries of the finite elements. A slip fluid–structure-interaction method is also proposed through the interface cells to enhance the computational accuracy of water-entry problems.

The validity and accuracy of the IALEFEM are verified by several benchmark numerical examples. The shock-cylinder obstacle interaction and flexible panel deformation induced by shock wave problems are studied to validate the IALEFEM in simulating compressible fluid–structure interaction. The water flow through a rubber plate problem is simulated to examine the ability of IALEFEM to handle incompressible fluid–structure interaction problems with large structural deformation, and the water entry of a wedge problem is studied to test the slip fluid–structure interaction method. The fragmentation of a cylinder shell induced by blast is used to simulate complicated FSI problems with structural fragmentation and high pressure explosive. The response of elastic plate subjected to spherical near-field explosion examines the capability of IALEFEM in solving 3D large structural deformation under explosion, while the structural damage of open-frame building under blast loading demonstrates the effectiveness and accuracy of the IALEFEM in simulating complex fluid–structure interaction problems with structural damage and multi-phase fluid flow. Numerical results are in good agreement with the experimental data and numerical data of other FSI methods.

For future directions, further consideration should be given to water-entry problems involving cavitation [97], structural damage and gas–liquid solid effects [64], since the FEM boundary provides accurate solid surface which is important for simulating water-entry problems. Other elements such as the solid shell elements, could also be considered to enhance the accuracy and efficiency of the IALEFEM. Moreover, the computational efficiency of IALEFEM is affected by the time-consuming intersection based remapping of MMALE grid, which requires parallel computing with GPU acceleration. The IALEFEM should also be combined with particle methods to simulate extreme deformation problems.

CRediT authorship contribution statement

Zixian Sun: Writing – review & editing, Writing – original draft, Visualization, Validation, Software, Methodology, Investigation, Formal analysis, Data curation, Conceptualization. **Zhixin Zeng:** Writing – review & editing. **Jiasheng Li:** Writing – review & editing. **Xiong Zhang:** Writing – review & editing, Supervision, Resources, Project administration, Funding acquisition.

Declaration of competing interest

We declare that we have no financial and personal relationships with other people or organizations that can inappropriately influence our work, there is no professional or other personal interest of any nature or kind in any product, service and/or company that could be construed as influencing the position presented in, or the review of, the manuscript.

Data availability

Data will be made available on request.

References

[1] S. Bandara, K. Soga, Coupling of soil deformation and pore fluid flow using material point method, Comput. Geotech. 63 (2015) 199–214.
[2] G. Ma, H.H. Bui, Y. Lian, K.M. Tran, G.D. Nguyen, A five-phase approach, SPH framework and applications for predictions of seepage-induced internal erosion and failure in unsaturated/saturated porous media, Comput. Methods Appl. Mech. Engrg. 401 (2022) 115614.
[3] Z. Wang, M. Soomro, C. Peng, L.F. Ayala, O.M. Ayala, Two pressure boundary conditions for multi-component multiphase flow simulations using the pseudo-potential lattice Boltzmann model, Comput. & Fluids 248 (2022) 105672.
[4] W. Liang, J. Zhao, H. Wu, K. Soga, Multiscale, multiphysics modeling of saturated granular materials in large deformation, Comput. Methods Appl. Mech. Engrg. 405 (2023) 115871.
[5] J. Zhang, S. Chen, H. Liu, Partitioned analysis of acoustic fluid-solid-saturated porous medium interaction problems by a generalized saturated porous medium model and localized Lagrange multipliers, Comput. Geotech. 170 (2024) 106271.
[6] Q. Zhu, F. Xu, S. Xu, M.-C. Hsu, J. Yan, An immersogeometric formulation for free-surface flows with application to marine engineering problems, Comput. Methods Appl. Mech. Engrg. 361 (2020) 112748.
[7] D. Yan, T. Mikkola, A. Lakshmynarayanana, S. T"odter, T.E. Schellin, J. Neugebauer, O. el Moctar, S. Hirdaris, A study into the FSI modelling of flat plate water entry and related uncertainties, Mar. Struct. 86 (2022) 103296.
[8] W.-S. Jang, W.-S. Choi, H.-G. Choi, S.-Y. Hong, J.-H. Song, Fatigue damage prediction of ship rudders under vortex-induced vibration using orthonormal modal FSI analysis, Mar. Struct. 88 (2023) 103376.
[9] R. Deiterding, F. Cirak, S. Mauch, Efficient fluid-structure interaction simulation of viscoplastic and fracturing thin-shells subjected to underwater shock loading, in: Theory, Numerics and Applications, 2008, pp. 283–294.
[10] A. Chaudhuri, A. Hadjadj, A. Chinnayya, On the use of immersed boundary methods for shock/obstacle interactions, J. Comput. Phys. 230 (5) (2011) 1731–1748.
[11] R. Ni, J. Li, X. Zhang, X. Zhou, X. Cui, An immersed boundary-material point method for shock-structure interaction and dynamic fracture, J. Comput. Phys. 470 (2022) 111558.
[12] A. Franci, E. Onate, J. Maria Carbonell, M. Chiumenti, PFEM formulation for thermo-coupled FSI analysis. Application to nuclear core melt accident, Comput. Methods Appl. Mech. Engrg. 325 (2017) 711–732.
[13] G. Li, J. Gao, P. Wen, Q. Zhao, J. Wang, J. Yan, A. Yamaji, A review on MPS method developments and applications in nuclear engineering, Comput. Methods Appl. Mech. Engrg. (ISSN: 0045-7825) 367 (2020) 113166.
[14] C.-C. Yu, F.U.H. Mir, A.S. Whittaker, Validation of numerical models for seismic fluid-structure-interaction analysis of nuclear, safety-related equipment, Nucl. Eng. Des. 379 (2021) 111179.

[15] Z. Ma, L. Qian, P. Martínez-Ferrer, D. Causon, C. Mingham, W. Bai, An overset mesh based multiphase flow solver for water entry problems, Comput. & Fluids 172 (2018) 689–705.
[16] I. Hammani, S. Marrone, A. Colagrossi, G. Oger, D. Le Touze, Detailed study on the extension of the delta-SPH model to multi-phase flow, Comput. Methods Appl. Mech. Engrg. 368 (2020) 113189.
[17] W.-T. Liu, A.-M. Zhang, X.-H. Miao, F.-R. Ming, Y.-L. Liu, Investigation of hydrodynamics of water impact and tail slamming of high-speed water entry with a novel immersed boundary method, J. Fluid Mech. 958 (2023).
[18] W. Noh, Cel: a time-dependent, two-space-dimensional, coupled Eulerian-Lagrangian code, Fundam. Methods Hydrodyn. (Methods Comput. Phys.) 3 (1964) 117–179.
[19] C. Chen, W.-K. Shi, Y.-M. Shen, J.-Q. Chen, A.-M. Zhang, A multi-resolution SPH-FEM method for fluid-structure interactions, Comput. Methods Appl. Mech. Engrg. 401 (2022) 115659.
[20] Y.-X. Peng, A.-M. Zhang, F.-R. Ming, Numerical simulation of structural damage subjected to the near-field underwater explosion based on SPH and RKPM, Ocean Eng. 222 (2021) 108576.
[21] Y. Liu, H. Ye, H. Zhang, Y. Zheng, Coupling phase-field LB-MP method for multiphase fluid-deformable solid interaction problems involving large density and viscosity contrasts, Int J Appl Mech 15 (06) (2023) 2350050.
[22] H.S. Udaykumar, W. Shyy, M.M. Rao, Elafint: A mixed Eulerian–Lagrangian method for fluid flows with complex and moving boundaries, Internat. J. Numer. Methods Fluids 22 (8) (2015) 691–712.
[23] T. Dunne, An Eulerian approach to fluid-structure interaction and goal-oriented mesh adaptation, Internat. J. Numer. Methods Fluids 51 (9–10) (2010) 1017–1039.
[24] C. F"orster, W.A. Wall, E. Ramm, Artificial added mass instabilities in sequential staggered coupling of nonlinear structures and incompressible viscous flows, Comput. Methods Appl. Mech. Engrg. 196 (7) (2007) 1278–1293.
[25] C.W. Hirt, A.A. Amsden, J.L. Cook, An arbitrary Lagrangian–Eulerian computing method for all flow speeds, J. Comput. Phys. 14 (2) (1974) 227–253.
[26] J. Donea, S. Giuliani, J.P. Halleux, An arbitrary Lagrangian–Eulerian finite element method for transient dynamic fluid-structure interactions, Comput. Methods Appl. Mech. Engrg. 33 (1–3) (1982) 689–723.
[27] A.J. Barlow, P.-H. Maire, W.J. Rider, R.N. Rieben, M.J. Shashkov, Arbitrary Lagrangian–Eulerian methods for modeling high-speed compressible multimaterial flows, J. Comput. Phys. 322 (2016) 603–665.
[28] J.-L. Pfister, O. Marquet, M. Carini, Linear stability analysis of strongly coupled fluid-structure problems with the arbitrary-Lagrangian–Eulerian method, Comput. Methods Appl. Mech. Engrg. 355 (2019) 663–689.
[29] G. Anjos, N. Mangiavacchi, J. Thome, An ALE-FE method for two-phase flows with dynamic boundaries, Comput. Methods Appl. Mech. Engrg. 362 (2020) 112820.
[30] J.A. González, K. Park, Three-field partitioned analysis of fluid-structure interaction problems with a consistent interface model, Comput. Methods Appl. Mech. Engrg. 414 (2023) 116134.
[31] T.E. Tezduyar, Stabilized finite element formulations for incompressible flow computations, Adv. Appl. Mech. 28 (28) (1991) 1–44.
[32] B. H"ubner, E. Walhorn, D. Dinkler, A monolithic approach to fluid-structure interaction using space-time finite elements, Comput. Methods Appl. Mech. Engrg. 193 (23–26) (2004) 2087–2104.
[33] S. Reinst"adler, U. Kowalsky, D. Dinkler, Analysis of landslides employing a space-time single-phase level-set method, Comput. Methods Appl. Mech. Engrg. 347 (2019) 639–662.
[34] S. Dutta, C.S. Jog, A monolithic, finite element-based strategy for solving fluid structure interaction problems coupled with electrostatics, Comput. & Fluids (2023) 264.
[35] J.S. Peery, D.E. Carroll, Multi-material ALE methods in unstructured grids, Comput. Methods Appl. Mech. Engrg. 187 (3–4) (2000) 591–619.
[36] X. Chen, X. Zhang, An improved 2D MoF method by using high order derivatives, J. Comput. Phys. 349 (2017) 176–190.
[37] H.T. Ahn, M. Shashkov, Multi-material interface reconstruction on generalized polyhedral meshes, J. Comput. Phys. 226 (2) (2007) 2096–2132.
[38] X. Chen, X. Zhang, Z. Jia, A robust and efficient polyhedron subdivision and intersection algorithm for three-dimensional MMALE remapping, J. Comput. Phys. 338 (2017) 1–17.
[39] X. Chen, X. Zhang, A coupled MMALE-FE method for solving 3D fluid-solid interaction problems with multi-material flow, Eng. Comput. 36 (8) (2019) 2766–2786.
[40] C.S. Peskin, Flow patterns around heart valves: A numerical method, J. Comput. Phys. 10 (2) (1972) 252–271.
[41] L. Zhang, A. Gerstenberger, X. Wang, W. Liu, Immersed finite element method, Comput. Methods Appl. Mech. Engrg. 193 (2004) 2051–2067.
[42] X. Wang, L.T. Zhang, Modified immersed finite element method for fully-coupled fluid-structure interactions, Comput. Methods Appl. Mech. Engrg. 267 (2013) 150–169.
[43] A. Neofytou, F. Yu, L.T. Zhang, H.A. Kim, Level set topology optimization for fluid-structure interactions, in: AIAA Scitech 2021 Forum, 2021.
[44] N.S. Nanal, S.T. Miller, J.D. Thomas, L.T. Zhang, Fluid-shell structure interactions with finite thickness using immersed method, Comput. Methods Appl. Mech. Engrg. 403 (2023).
[45] C. Jiang, J.-Y. Yao, Z.-Q. Zhang, G.-J. Gao, G. Liu, A sharp-interface immersed smoothed finite element method for interactions between incompressible flows and large deformation solids, Comput. Methods Appl. Mech. Engrg. 340 (2018) 24–53.
[46] M.-J. Li, Y. Lian, X. Zhang, An immersed finite element material point (IFEMP) method for free surface fluid-structure interaction problems, Comput. Methods Appl. Mech. Engrg. 393 (2022) 114809.
[47] B. Schott, C. Ager, W.A. Wall, A monolithic approach to fluid-structure interaction based on a hybrid Eulerian-ALE fluid domain decomposition involving cut elements, Internat. J. Numer. Methods Fluids 08 (2018).
[48] J. Kim, C. Lee, H.-G. Kim, S. Im, The surrounding cell method based on the S-FEM for analysis of FSI problems dealing with an immersed solid, Comput. Methods Appl. Mech. Engrg. 341 (2018) 658–694.
[49] L. Kan, X. Zhang, An immersed MMALE material point method for FSI problems with structure fracturing, Comput. Methods Appl. Mech. Engrg. 396 (2022) 115099.
[50] Z. Sun, R. Ni, Z. Zeng, X. Zhang, A localized subdomain smoothing MMALE particle method for efficient modeling FSI problems, Comput. Methods Appl. Mech. Engrg. 419 (2024) 116676.
[51] T. Kolev, R. Rieben, A tensor artificial viscosity using a finite element approach, J. Comput. Phys. 228 (2009) 8336–8366.
[52] E. Caramana, M. Shashkov, P. Whalen, Formulations of artificial viscosity for multi-dimensional shock wave computations, J. Comput. Phys. 144 (1998) 70–97.
[53] E. Caramana, M. Shashkov, Elimination of artificial grid distortion and hourglass-type motions by means of Lagrangian subzonal masses and pressures, J. Comput. Phys. 142 (1998) 521–561.
[54] X. Xu, A parameter-free staggered-grid Lagrangian scheme for two-dimensional compressible flow problems, J. Comput. Phys. 499 (2024) 112720.
[55] M. Shashkov, Closure models for multimaterial cells in arbitrary Lagrangian–Eulerian hydrocodes, Internat. J. Numer. Methods Fluids 56 (2008) 1479–1504.
[56] E.J. Caramana, C.L. Rousculp, D.E. Burton, A compatible, energy and symmetry preserving Lagrangian hydrodynamics algorithm in three-dimensional cartesian geometry, J. Comput. Phys. 157 (1) (2000) 89–119.
[57] A. Barlow, R. Hill, M. Shashkov, Constrained optimization framework for interface-aware sub-scale dynamics closure model for multimaterial cells in Lagrangian and arbitrary Lagrangian–Eulerian hydrodynamics, J. Comput. Phys. 276 (2014) 92–135.

[58] Y.V. Yanilkin, E.A. Goncharov, V.Y. Kolobyanin, V.V. Sadchikov, W.J. Rider, Multi-material pressure relaxation methods for Lagrangian hydrodynamics, Comput. & Fluids 83 (17) (2013) 137–143.
[59] R.E. Tipton, CALE mixed zone pressure relaxation, Pers. Not. (1989) unpublished.
[60] M. Kucharik, R. Garimella, S.P. Schofield, M. Shashkov, A comparative study of interface reconstruction methods for multi-material ALE simulations, J. Comput. Phys. 229 (2010) 2432–2452.
[61] J.S. Peery, D.E. Carroll, Multi-material ALE methods in unstructured grids, Comput. Methods Appl. Mech. Engrg. 187 (3/4) (2000) 591–619.
[62] Z. Jia, J. Liu, S. Zhang, An effective integration of methods for second-order three-dimensional multi-material ALE method on unstructured hexahedral meshes using MOF interface reconstruction, J. Comput. Phys. 236 (2013) 513–562.
[63] P. Knupp, L.G. Margolin, M. Shashkov, Reference Jacobian optimization-based rezone strategies for arbitrary Lagrangian Eulerian methods, J. Comput. Phys. 176 (1) (2002) 93–128.
[64] M. Cao, Z. Shao, S. Wu, C. Dong, X. Yang, Numerical and experimental study of cone-headed projectile entering water vertically based on MMALE method, Int. J. Nav. Archit. Ocean Eng. 13 (2021) 877–888.
[65] X. Chen, X. Zhang, An improved 3D MoF method based on analytical partial derivatives, J. Comput. Phys. 326 (2016) 156–170.
[66] S. Galera, J. Breil, P.-H. Maire, A 2D unstructured multi-material cell-centered arbitrary Lagrangian–Eulerian (CCALE) scheme using MOF interface reconstruction, Comput. & Fluids 46 (1) (2011) 237–244.
[67] H. Ahn, M. Shashkov, Multi-material interface reconstruction on generalized polyhedral meshes, J. Comput. Phys. 226 (2007) 2096–2132.
[68] Z. Jia, J. Liu, S. Zhang, An effective integration of methods for second-order three-dimensional multi-material ALE method on unstructured hexahedral meshes using MOF interface reconstruction, J. Comput. Phys. 236 (2013) 513–562.
[69] Peskin, S. Charles, The immersed boundary method, Acta Numer. 11 (2002) 479–517.
[70] D.P. Flanagan, T. Belytschko, A uniform strain hexahedron and quadrilateral with orthogonal hourglass control, Internat. J. Numer. Methods Engrg. 17 (1981) 679–706.
[71] Z. Chen, X. Qiu, X. Zhang, Y. Lian, Improved coupling of finite element method with material point method based on a particle-to-surface contact algorithm, Comput. Methods Appl. Mech. Engrg. 293 (2015) 1–19.
[72] A.E. Bryson, R. Gross, Diffraction of strong shocks by cones, cylinders, and spheres, J. Fluid Mech. 10 (01) (1961) 1–16.
[73] J. Giordano, G. Jourdan, Y. Burtschell, M. Medale, D. Zeitoun, L. Houas, Shock wave impacts on deforming panel, an application of fluid-structure interaction, Shock Waves 14 (2005) 103–110, http://dx.doi.org/10.1007/s00193-005-0246-9.
[74] L. Wang, G. Currao, F. Han, A. Neely, J. Young, F.-B. Tian, An immersed boundary method for fluid-structure interaction with compressible multiphase flows, J. Comput. Phys. 346 (2017) 131–151, http://dx.doi.org/10.1016/j.jcp.2017.06.008.
[75] C. Antoci, M. Gallati, S. Sibilla, Numerical simulation of fluid-structure interaction by SPH, Comput. Struct. 85 (11) (2007) 879–890.
[76] J.P. Morris, P.J. Fox, Y. Zhu, Modeling low Reynolds number incompressible flows using SPH, J. Comput. Phys. 136 (1) (1997) 214–226.
[77] A. Rafiee, K.P. Thiagarajan, An SPH projection method for simulating fluid-hypoelastic structure interaction, Comput. Methods Appl. Mech. Engrg. 198 (33) (2009) 2785–2795.
[78] Q. Yang, V. Jones, L. McCue, Free-surface flow interactions with deformable structures using an SPH-FEM model, Ocean Eng. 55 (2012) 136–147.
[79] A. Khayyer, H. Gotoh, H. Falahaty, Y. Shimizu, An enhanced ISPH-SPH coupled method for simulation of incompressible fluid-elastic structure interactions, Comput. Phys. Comm. 232 (2018) 139–164.
[80] R. Zhao, O. Faltinsen, J. Aarsnes, Water entry of arbitrary two-dimensional sections with and without flow separation, in: Proceedings of the 21st Symposium on Naval Hydrodynamics, National Academy Press, Trondheim, Norway, Washington, DC, USA, 1996, pp. 408–423.
[81] J.P. Morris, P.J. Fox, Y. Zhu, Modeling low Reynolds number incompressible flows using SPH, J. Comput. Phys. 136 (1) (1997) 214–226.
[82] Y. Zhang, A level set immersed boundary method for water entry and exit, Commun. Comput. Phys. 8 (2010) 265–288.
[83] T. Tang, Y. Gu, Q. Li, J. Hua, X. Sun, Expanding fracture of steel cylinder shell by detonation drivings, Explos. Shock Waves 23 (6) (2003) 529–533.
[84] P. Yang, Y. Liu, X. Zhang, X. Zhou, Y. Zhao, Simulation of fragmentation with material point method based on gurson model and random failure, CMES - Comput. Model. Eng. Sci. 85 (2012) 207–237.
[85] H.S. Dong, High Energy Explosive and Some Related Properties, Sceience Press, Beijing, 1989.
[86] G. Chen, Z. Chen, W. Xu, Y. Chen, X. Huang, Investigation on the J-C ductile fracture parameters of 45 steel, Explos. Shock Waves 27 (2) (2007) 131–135.
[87] A.L. Gurson, Continuum theory of ductile rupture by void nucleation and growth: Part I - yield criteria and flow rules for porous ductile media, J. Eng. Mater. Technol. 99 (1) (1977) 297–300.
[88] X. Lin, S.C. Fong, Ductile crack growth - II. Void nucleation and geometry effects on macroscopic fracture behavior, J. Mech. Phys. Solids 43 (12) (1995) 1953–1981.
[89] A. Neubergera, S. Peles, D. Rittel, Scaling the response of circular plates subjected to large and close-range spherical explosions. Part I air-blast loading, Int. J. Impact Eng. 32 (2007) 859–873.
[90] M.B. Liu, G. Liu, K.Y. Lam, Meshfree particle simulation of the detonation process for high explosive in shaped unlined cavity configurations, Shock Waves 12 (6) (2003) 509–520.
[91] Meyers, Dynamic Behavior of Materials, John Wiley and Son, 1994.
[92] S.C. Woodson, J.T. Baylot, Structural Collapse: Quarter-Scale Model Experiments, Technical Report SL-99-8, US Army ERDC, 1999.
[93] J.T. Baylot, T.L. Bevins, Effect of responding and failing structural components on the airblast pressures and loads on and inside of the structure, Comput. Struct. 85 (11–14) (2007) 891–910.
[94] Y. Shi, H. Hao, Z.-X. Li, Numerical derivation of pressure-impulse diagrams for prediction of RC column damage to blast loads, Int. J. Impact Eng. 35 (11) (2008) 1213–1227.
[95] W. Chen, H. Hao, S. Chen, Numerical analysis of prestressed reinforced concrete beam subjected to blast loading, Mater. Design (1980-2015) 65 (2015) 662–674.
[96] H. Li, L. Li, M. Ye, M. Li, Y. Wu, Blast fragility assessment of aging coastal RC columns exposed to non-uniform CIC attacks using LBE function, J. Build. Eng. 71 (2023) 106510.
[97] A.-M. Zhang, S.-M. Li, P. Cui, S. Li, Y.-L. Liu, A unified theory for bubble dynamics, Phys. Fluids 35 (3) (2023) 033323.